# Edge-effet: Liquid sheet and droplets formed by a drop impacting close to an edge

S. Lejeune*
*Microfluidics Lab, Department of Aerospace and Mechanical Engineering, University of Liège, Liège, Belgium and The Fluid Dynamics of Disease Transmission Laboratory, Massachusetts Institute of Technology, Cambridge, MA 02139, US*

T. Gilet†
*Microfluidics Lab, Department of Aerospace and Mechanical Engineering, University of Liège, Liège, Belgium*

L. Bourouiba‡
*The Fluid Dynamics of Disease Transmission Laboratory, Massachusetts Institute of Technology, Cambridge, MA 02139, US*
(Dated: December 19, 2017)

Asymmetric liquid sheet fragmentation are ubiquitous in nature and potentially shapes critical phenomenon such as rain-induced propagation of foliar diseases. In this experimental study, we propose a configuration that allows for the study of such asymmetric liquid sheet in the plane through the variation of the impact Weber number and the asymmetry parameter, captured by the offset. The effects of their variation on the kinematics of the liquid sheet behaviour is described qualitatively and quantitatively. Three major asymmetry scenarios are identified and linked to distinct drop ejection pattern. Scaling laws are proposed to rationalise the scenarios based on the impact parameters.

## I. INTRODUCTION

Around 10% of the world crops are still lost due to plant diseases [1] which costs billions of dollars each year [2, 3] and increases pressure on communities [1]. The optimization of timings and amounts of sprayed chemicals in the context of smart agriculture requires improved understanding of disease spread in the field [4–7]. Rain is correlated to the dispersal of foliar diseases such as the septoria leaf blotch and the fusarium head blight affecting wheat and rice respectively [8–10]. Previous studies have attempted to rationalize the underlying mechanisms, but they mainly focused on dispersal statistics collected at the level of plant and crop field [9, 11–13]. Investigations at the level of leafs and raindrops are scarce [11, 14–16]. They are mostly conducted based on statistical droplet collection, neither accounting for the drop-plant interaction nor for the fragmentation physics. Thus generalizing these studies to various plants and types of rain remains challenging [7, 17]. Recent studies have shed new insights on raindrop-leaf interactions [18, 19], identifying the important role of sessile drops on leaves and the several dispersal mechanisms that are both common and efficient at dispersing pathogens. One of the main dispersal scenario on semi-rigid leaves, coined *crescent-moon* (figure 1a), consists in the impact of a raindrop in the vicinity of a sessile (contaminated) drop supported by the infected leaf. The sessile drop is stretched into an asymmetric liquid sheet, which then retracts and fragments into a myriad of contaminated droplets ejected away from the plant.

Drop impacts have been studied in many configurations [20–22] including drop impacts on thin films [23–25], on deep liquid layers [26, 27], or solid substrates with various wetting properties, geometry and inclination [21, 28–32]. Impacts at sufficiently high speed result in a splash, which involves the formation of a liquid sheet, a crown, which then destabilizes into droplets. Many studies focused on the crown dynamics and on the conditions leading to droplet ejection, often in axisymmetric configurations [33–37]. Increasing attention has also been paid to impacts on small solid targets (of comparable size to that of the drop diameter) [38–41] or binary drop collision [42, 43]. In the *crescent-moon* impact scenario, an intrinsic horizontal asymmetry leads to a non-axisymmetric liquid sheet [19]. This latter induces asymmetry in the speed and direction of ejected droplets. Inclination, compliance and finite size of the leaves all amplify this asymmetry. Drop impacts were studied in other configurations that yield asymmetric behaviors: (i) with horizontal gradients of texture and wetting properties [44–49], (ii) with varying inclination or tangential speed of the substrate [50–52], and (iii) with non-axisymmetric target shapes [53, 54]. Yet none of these studies looked into the relationship between liquid sheet asymmetry and subsequent droplet ejections. Moreover, the distribution of speed

* slejeune@uliege.be
† tristan.gilet@uliege.be
‡ lbouro@mit.edu

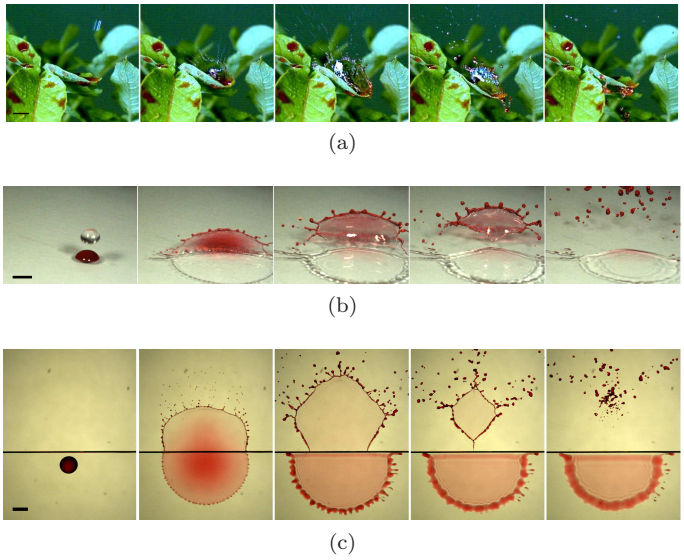

FIG. 1. Liquid sheet formation and fragmentation into droplets, in three configurations: (a) In-field: a raindrop impacts onto a potato leaf on which dyed fluid (red) was deposited. Times are, from left to right, -3, 2, 6, 13 and 29 ms after impact. The sheet is fully three-dimensional. (b) A water drop impacts close to a dyed sessile drop on a flat dry plexiglass substrate. Times are, from left to right, -1, 3, 8, 11 and 23 ms after impact. The sheet is still fully 3D. (c) Impact of a dyed drop close the edge of a flat dry plexiglass substrate. Times are, from left to right, 0, 2.5, 8, 10.5 and 14 ms after impact. The sheet remains in the plane of the substrate. Scale bars are 5 mm.

and direction of the ejected droplets was rarely reported, though these variables are crucial to assess the capability of raindrops to disperse plant diseases.

The observation of a large number of drop impacts on wet leaves, in fields and in the lab (figure 1a and 1b), confirmed the frequent occurrence of asymmetric liquid sheets in the air. These sheets develop either through the *crescent-moon* scenario described in Gilet and Bourouiba [18], or by impacts close to the edges of the leaves, or through a combination of both. The *crescent-moon* mechanism was reproduced in lab conditions with a drop impacting close to a sessile drop on a flat, dry and rigid plexiglass plate (figure 1b). The key emerging features are: (i) the asymmetric shape of the sheet in the air, (ii) the fluid of this sheet originating mainly from the sessile drop, (iii) a free destabilising rim at the outer-edge of the sheet, and (iv) the presence a triple contact line solid-liquid-air at the junction with the substrate, which can be fixed (e.g. the edge of the leaf) or be formed by the lift of the sheet from the substrate (e.g. in the *crescent-moon* scenario). The *crescent-moon* sheet is inherently three-dimensional, hence complicated to track accurately.

In this paper, we identify and study one of the simplest impact configurations that produces a sheet with the aforementioned features. It consists in the impact of a single drop close to the straight edge of a flat dry plexiglass plate (figure 1c). Upon impact, the drop spreads radially until it reaches the edge. It then continues to expand in the air, thereby forming a liquid sheet whose asymmetry varies with the distance from the impact point to the edge.

The main goal of this paper is to characterize both the dynamics of this sheet and the number, mass, direction and speed of the ejected droplets, as a function of impact speed and the distance of impact point to the edge. In section II, we first present the experimental setup. We then describe the phenomenology of liquid sheet expansion, retraction and break-up for various impact speeds and asymmetries in section III. A quantitative analysis of the sheet dynamics and the droplet statistics is presented in sections IV and V, respectively. Results and implications of the asymmetry of the liquid sheet in shaping droplet patterns in the context of rain-induced foliar pathogen dispersal are discussed in the last section.

## II. EXPERIMENTAL SETUP

A syringe pump is filled with dyed water, of surface tension $\sigma \simeq 70$ mN/m, density $\rho \simeq 1000$ kg/m$^3$ and kinematic viscosity $\nu \simeq 10^{-6}$ m$^2$/s at room temperature ($22 \pm 2$°C). The syringe is connected to a vertical needle that releases drops of radius $R_0$ $2.4 \pm 0.03$ mm. These drops fall and impact near the edge of a flat horizontal substrate. . This substrate is made of dry plexiglass, 2 mm thick, with advancing and receding contact angles of 85° and 55° ($\pm 15$°),

TABLE I. List of symbols used together with typical values

| *Symbol* | *Meaning* | *Value/Range* (room T° $\simeq 20°C$) |
|---|---|---|
| $d$ | offset | 2.4 - 12 mm |
| $R_0$ | initial drop radius | 2.4±0.03 mm |
| $V_0$ | initial drop speed | 1.6, 2.3, 3.2, 4.4, 6 ±0.1 m/s |
| $\rho$ | water density | 1000 kg/m$^3$ |
| $\nu$ | water kinematic viscosity | $10^{-6}$ m$^2$/s |
| $\sigma$ | water surface tension | 70 mN/m |
| $t_i$ | impact time | 2.9, 2.1, 1.5, 1.1, 0.8 ms |
| $t_c$ | capillary time | 16 ms |
| $We$ | Weber number | 186 (◯), 367 (▷), 700 (★), 1340 (□), 2435 (♢) |
| $Oh$ | Ohnesorge number | 0.0017 |

respectively, cut straight with average roughness $\simeq 4\mu$m. The offset $d$ is defined as the distance between the impact point and the straight edge, counted positively when at least half the drop hits the substrate. It is varied in the range $d/R_0 \in [-1, 5]$ thanks to a millimetre stage.Parameters are summarised in table I. The phenomenon is recorded from the top with a high speed camera (MIRO 340 from Phantom , Inc.) and using backlighting at 2000 frames per second. The inclination of the camera is less than 20° from the vertical, and is accounted for in the image processing. The position and shape of both the liquid sheet and the droplets are measured by image processing. Time interpolations of these motions allowed for a detection of major events such as the impact of the drop and the entry of the sheet in the air.

Five different impact speeds $V_0$ in the range $1.6 - 6$ m/s were tested by changing the height of the needle (table I). The impact speed was determined as a function of the height of release in a different experiment, where the falling drops were filmed from the side. Slight oscillations and flattening of the incoming drop, observed during the free fall right before impact, did not appear to affect the impact dynamics at first order.

Figure 1c shows the process from impact to sheet collapse over 12.5 ms. The impact time of the drops scales as $t_i = 2R_0/V_0 \simeq 1$ ms (table I). The sheet lifetime is closer to the capillary time $t_c = \sqrt{4\rho R_0^3/(3\sigma)} = 16.2$ ms. The Weber number $We = 2\rho R_0 {V_0}^2/\sigma = (t_i/t_c)^2$, representing the kinetic energy of the impacting drop divided by its surface energy, is much larger than unity in all our experiments (table I). The Froude number squared $Fr = V_0^2/(2gR_0)$ ranges between 50 and 800, allowing to neglect hydrostatic pressure.

Viscous effects can be neglected during impact given that the Ohnesorge number $Oh = \sqrt{\nu^2\rho/(2R_0\sigma)}$ is 0.0017 for the considered size of the impacting drop. In rainfalls, the diameter and terminal speed of raindrops range from 0.5 mm at 2 m/s to 5 mm at 9 m/s, respectively [55, 56]. These parameters yield $We \in [28, 5800]$, $Fr \in [800, 1700]$ and $Oh \in [0.0017, 0.0053]$. These ranges for rainfalls are fairly close to those considered in this lab experiment, so it can be assumed that the dominant effects (inertia and surface tension) and negligible effects (gravity, viscosity) will be the same in both configurations.

## III. PHENOMENOLOGY

In figure 2, the impact near an edge is presented from top view and simultaneous side views are presented below. Along the edge, the extension of the liquid sheet in the air follows the spreading on solid (figure 2b-d). By contrast, the strong retraction of the sheet along the edge is desynchronised from the slight dewetting on top of the substrate (figure 2e-g). In the direction normal to the edge, the sheet extends further in the air than it spreads on the solid (figure 2b-d). The maximum extension of the sheet is reached first along the edge then normal to the edge (figure 2e). The differences in these extension and retraction kinematics normal and tangent to the edge are key in shaping the asymmetric liquid sheet in the air. Droplets are emitted from the corrugated rim at the front of the sheet, as well as from the break-up of the filaments after the collapse of the sheet.

The side view in figure 2 shows that the sheet stays approximately in the plane of the substrate throughout the whole process. The droplets are also ejected in this plane, except during the final collapse of the sheet where the antagonist movements of the rim along the edge give rise to out-of-plane ejections (figure 2g-h-side views). The planar and almost horizontal movements of the sheet are crucial for the accuracy of geometric and kinematic measurements from the top view alone. We measured the inclination $\varphi$ from the vertical of the sheet at its maximal expansion, as a function of $d$ (figure 3). This inclination first increases linearly with $d/R_0$ and then reaches a plateau of mean value 87°, independent of We. This value below 90° could be explained by the slight hydrophilicity of the substrate [57, 58] or by an imperfect transfer of momentum from vertical to horizontal during the initial crushing and was also noted

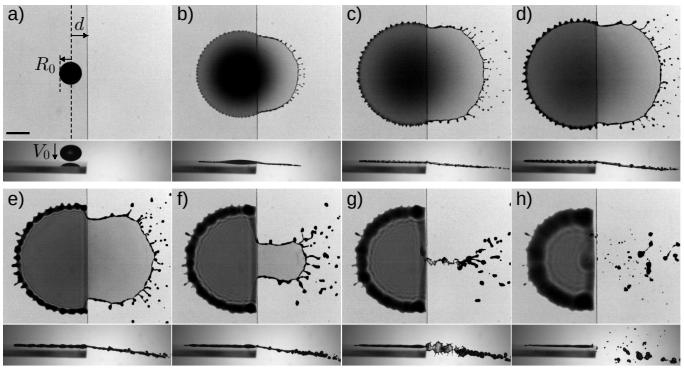


FIG. 2. Drop impact on a flat surface close to its edge, from top and side view. The radius of the impacting drop is $R_0 \simeq 2.4$ mm and the Weber number $We = 1300$. The offset $d$ is defined as the distance between the impact point and the edge. The scale bar is 5 mm and the times are t = 0 ms, 1.6 ms, 3 ms, 4.4 ms, 7 ms, 10.6 ms, 12.4 ms and 19 ms after impact.

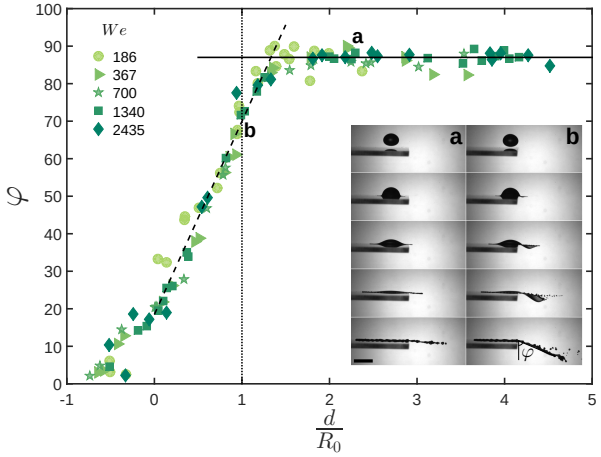


FIG. 3. Inclination $\varphi$ of the sheet with respect to the vertical as a function of the offset $d/R_0$ for different $We$ (see table I for symbols of We). The solid line is $\varphi = 87°$ and the long dotted line represents equation (1). Inset: Side-view time sequence of a drop impacting near an edge at We = 680, for $d/R_0 = 2.2$ (a) and $d/R_0 = 1$ (b). Images are taken at -0.4, 0, 0.4, 0.8, 2, 3.2 and 5.8 ms from the time of impact, respectively from top to bottom. The scale bar is 4 mm.

for symmetric impacts on poles [41]. A linear fit of the range $d/R_0 \in [0, 1]$ gives

$$\varphi \simeq 53\frac{d}{R_0} + 18. \tag{1}$$

The intersection of this fit with the plateau occurs at $d/R_0 \simeq 1.3$. For larger offsets, the sheet can be assumed to remain in the plane of the substrate (figure 3 - inset a). When $d/R_0 < 1.3$ (figure 3 - inset b), the deformation of the drop at initial crush brings part of the liquid beyond the edge. This creates a bulge and jeopardizes a planar sheet expansion. The bulge however resorbs during the retraction and the sheet becomes almost planar again but inclined. In the remainder of this paper, experiments with $d/R_0 < 1$, corresponding to the drop being cut by the edge, are systematically excluded.

Both the shape and the amount of liquid in the sheet vary with the offset. Figure 4 shows four impacts with the same $We$ but different $d/R_0$. The initial spreading on solid is obviously identical for all, and almost axisymmetric. With a smaller offset, the liquid reaches the edge and enters the air sooner and consequently at higher speed. The extension of the sheet in the air is faster than that on the solid in the perpendicular direction while it follows the extension speed of the solid tangentially to the edge. This anisotropy in extension causes a distortion of the sheet that becomes more pronounced as the offset decreases. The maximal extensions of the sheet in directions normal and tangential to the edge are reached at different times which strongly conditions the subsequent retraction. The rim at the front of the sheet becomes more corrugated and emits droplets sooner than the rim close to the edge (figure 4b).

As the offset is varied, a continuum of sheet kinematics is observed, among which three main scenario, with increasing

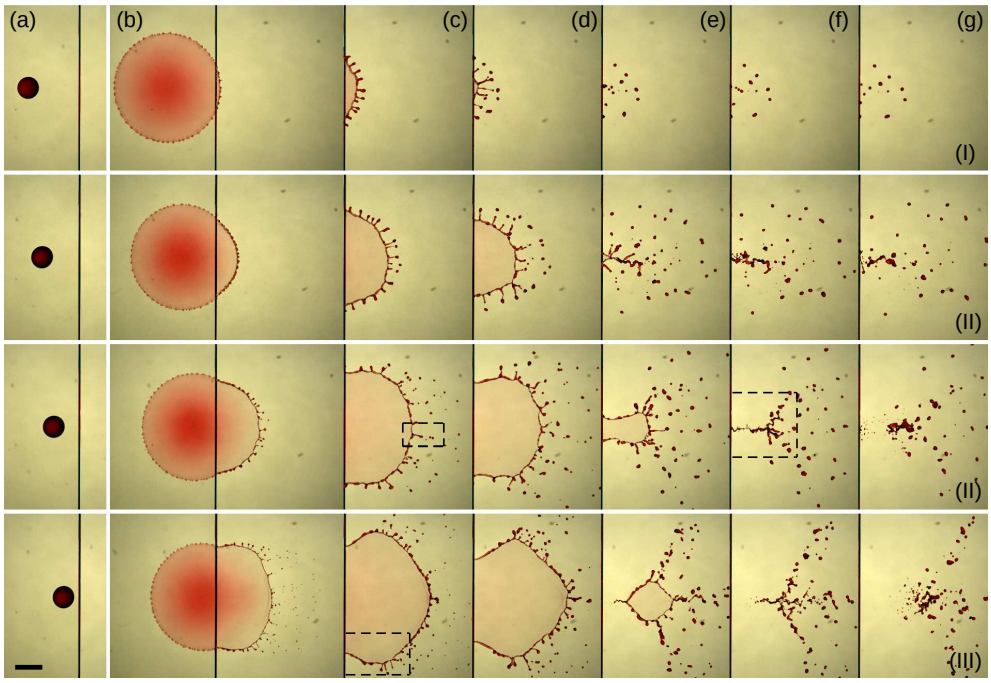


FIG. 4. Time evolution of the sheet in the air for $d/R_0 = 4.4$, 3.2, 2 and 1.3 (top to bottom) and $We = 1300$. Rows 1, 2, 3 and 4 correspond to the retraction scenario (I), (II), (II) and (III). Snapshots in a same column are taken at the same time $t$ post impact, with $t = 0$ ms, 3 ms, 6 ms, 8 ms, 11 ms, 12 ms, and 14 ms from top to bottom.(a) illustrates the position of the drops right before the impact, with respect to the edge. Scale bar is 5 mm. The dotted frames highlight three different droplets ejections mechanisms that will be later illustrated in figure 16.

asymmetry from scenario (I) to (III).

(I) When $d$ is sufficiently large (figure 4 - row 1), the maximum extension of the sheet is reached simultaneously along and normal to the edge. The shape of the sheet is approximately axisymmetric, in the continuation of the spreading on solid. The sheet retraction is also axisymmetric, as if the air was not present. Droplets are only emitted during this retraction phase.

(II) As $d$ decreases (figure 4 - rows 2 and 3), the maximum extension is both larger and reached later in the direction normal to the edge than tangentially to the edge. The retraction of the sheet is mostly dominated by the early motion tangent to the edge, the normal retraction being delayed. The final shape prior to collapse varies from a very small triangle attached to the edge to a rectangle with a width along the edge smaller than its length normal to it. The sheet collapses all at once into a filament (figure 4 - column 2e and 3f-g). The breakup of this filament generates droplets that are significantly smaller than those ejected otherwise.

(III) Finally at $d/R_0 \sim 1.3$ (figure 4 - row 4), the sheet anisotropy becomes very pronounced. The sheet takes a polygonal shape that is conserved during retraction. The retraction along the edge is completed while it has only started in the perpendicular direction. The sheet then pinches and separates from the edge before collapse. This pinching also generates a filament that breaks up into tiny droplets.

For a given offset, a variation of the impact speed (and corresponding Weber number) does not strongly modify the shape of the liquid sheet. Three examples of impacts taken at identical $d/R_0 \simeq 1.3$ and different speeds are illustrated in figure 5, all leading to scenario (III). Differences are nevertheless observed, both in terms of temporal evolution and size of the sheet. At higher impact speed, the maximal sheet expansion is larger, but it surprisingly collapses sooner. The ejected droplets are also smaller and ejected sooner.

## IV. SHEET DYNAMICS

The scenarios discussed in section III are first reported in an offset vs. Weber diagram (figure 6). The range of offset $d/R_0$ of each scenario decreases with decreasing $We$, down to $We = 186$ for which only the axisymmetric scenario (I)

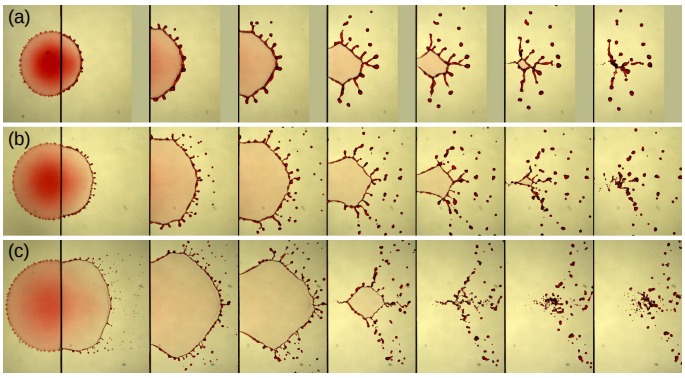


FIG. 5. Time evolution of the sheet in the air for $We = 350$, 680 and 1300 from top to bottom, for $d/R_0 = 1.3$. Snapshots in a same column are taken at the same time $t$ post impact, with t = 3 ms, 6 ms, 8 ms, 11 ms, 12 ms, 13 ms, and 14 ms from left to right. Scale bar is 5 mm.

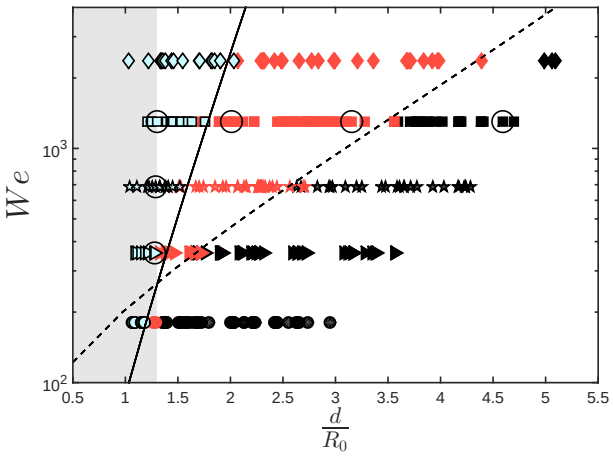


FIG. 6. Phase diagram $We$ vs. $d/R_0$, in which different sheet asymmetry scenario are colored differently: I (black), II (red) and III (blue).Symbols correspond to different $We$, according to table I. The data corresponding to the examples of figures 4 and 5 are circled. The shaded region $d/R_0 < 1.3$ corresponds to experiments for which the sheet is not planar. The solid and dashed lines correspond to equations (15) and (16), respectively.

subsists for $d/R_0 \geq 1.3$.

The sheet kinematics is quantified through the evolution of its extension $l_n(t)$ (resp. $l_t(t)$) in the direction normal to the edge (resp. tangential to the edge), as illustrated in figure 7. We also measured the spreading $R_s(t)$ of the liquid on the solid, since this motion is a prerequisite to the expansion of the sheet in the air. These measurements are performed automatically with custom image processing in ImageJ and Matlab. By convention, times are measured from the time of impact.

### A. Spreading on solid

Upon impact, the spreading radius $R_s(t)$ quickly increases and reaches a maximum $R_{sM}$ in a finite time $t_{sM}$ (figure 8a). Slight dewetting is then observed, due to the weak hydrophilicity of the substrate [59].

Previous analysis of the early times of spreading suggests an increase in radius proportional to $\sqrt{t}$ [59]. However, at later times the spreading dynamics involves several dissipation mechanisms and there is no simple model that fully describes its kinematics [59–63]. Consequently, we chose to fit an empirical function $R_s(t)$ that grows as $\sqrt{t}$ in the early times and saturates in a finite time:

$$\frac{R_s(t)}{R_{sM}} \simeq \sqrt{\frac{t}{t_{sM}}\left(2 - \frac{t}{t_{sM}}\right)} \tag{2}$$

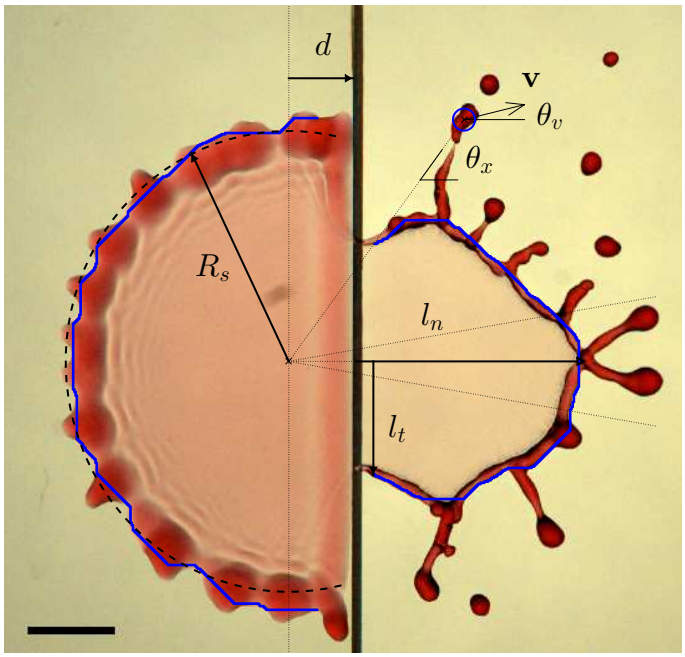


FIG. 7. Main variables that characterise the kinematics of the spreading on solid, liquid sheet in the air, and ejected droplets. The contours (blue lines) are detected by image processing, after thresholding and morphological removal of the corrugations. This particular image is taken 10.5 ms after impact, at offset $d/R_0 = 1.28$ and $We = 350$. Scale bar is 4 mm. The radius $R_s$ of the spreading liquid on solid, the extension of the liquid sheet tangent to the edge $l_t$ and the normal extension of the sheet $l_n$ are represented. This latter is taken to be the quantile 85% in distance to the edge of the contour of the sheet located in a sector of $\pm 10^o$ (fine dotted lines).

Both $R_{sM}$ and $t_{sM}$ are obtained by least square fitting for each individual impact.

The observed maximum spreading $R_{sM}$ increases with $We$ (figure 8a - left inset). This variation is well captured by the empirical law of Laan *et al.* [64]:

$$\frac{R_{sM}}{R_0} = \frac{We^{1/2}}{(1.14 + We^{2/5}Oh^{1/5})} \simeq 1.4We^{1/5} \tag{3}$$

where the constant 1.14 is a fitting parameter and $1.4We^{1/5}$ is a best fit approximation for the regime $(We, Oh)$ considered in this paper.

The time at which the spreading radius reaches its maximum also increases with $We$ (figure 8a - right inset). It can be adjusted with the power-law

$$t_{sM} = 0.8We^{1/4}t_i, \tag{4}$$

where 0.8 is a fitting parameters. The exponent 1/4 suggests that the time of maximum spreading is almost proportional to $\sqrt{V_0}$, as observed by Antonini *et al.* [30]. The alternative $t_{sM} \simeq 0.3We^{3/10}Oh^{-1/10}$ proposed by Lagubeau *et al.* [65] is also in good agreement with our data.

The normalised spreading radius $R_s/R_{sM}$ as a function of the normalised time $t/t_{sM}$ is shown in Figure 8b. Data from different $We$ collapse onto a single curve, which is very well approximated by equation (2) for $t < t_{sM}$. The match between the experimental curves and the equations is not valid beyond $t > t_{sM}$ as dewetting obeys a different dynamics that is sensitive to the surface properties of the substrate. From equation (2), we can predict the time $t_d$ at which the liquid arrives at the edge of the substrate ($R_s(t_d) = d$):

$$\frac{t_d}{t_{sM}} = (1 - \sqrt{1 - \delta^2}) \tag{5}$$

where $\delta = d/R_{sM} < 1$ is defined as the dimensionless offset. This equation is also in good agreement with the experimental measurements of the time of formation of the liquid sheet (figure 8b - inset).

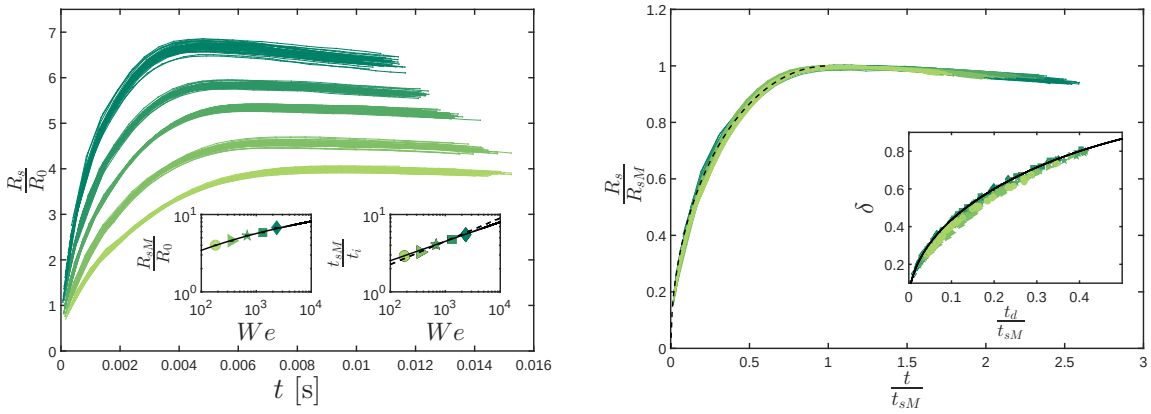


(a) (b)

FIG. 8. (a) Time evolution of the spreading radius $R_s/R_0$ for increasing $We$ (from bottom to top, $We = 180, 350, 680, 1300, 2600$). Insets show the maximum spreading $R_{sM}/R_0$ as a function of $We$. The solid line corresponds to (3) (Left). (Right) Time $t_{sM}/t_i$ of the maximum spreading as a function of $We$. The solid line corresponds to (4). The dotted line is the scaling $t_{sM}/t_i \simeq We^{3/10}Oh^{-1/10}$ from Lagubeau *et al.* [65]. (b) Rescaled time evolution of the spreading radius $R_s/R_{sM}$ vs. $t/t_{sM}$, for the five $We$ values in table I. The dotted line represents equation (2). Inset shows dimensionless offset $\delta = d/R_{sM}$ as a function of $t_d/t_{sM}$. The solid line corresponds to equation (5). Symbols correspond to different $We$, all collapsed from 186 to 2435.

### B. Expansion/retraction of the liquid sheet in the air, normal to the edge

As soon as it takes off from the edge, the liquid is not subject to the no-slip boundary condition on the substrate and to the subsequent shear. We therefore expect the expansion dynamics in the air to be different from that on the substrate. The extension of the sheet normal to the edge $l_n(t)$ is advantageously described by defining a dimensionless time

$$\tau_n = \frac{t - t_d}{t_{nM} - t_d}. \tag{6}$$

that corresponds to the time from fluid entry in the air $t - t_d$, divided by the time $t_{nM} - t_d$ of maximum extension in the air, normal to the edge. Similarly, the normal extension of the sheet is normalized by its maximal extension $l_{nM}$. With this normalization, all experimental data collapse onto a single curve approximated by

$$\frac{l_n}{l_{nM}} = \tau_n(2 - \tau_n), \tag{7}$$

as shown in figure 9a. The acceleration of the sheet normal to the edge is therefore constant during the whole extension and retraction.

Both $l_{nM}$ and $t_{nM}$ are obtained for each experiment by least-square fitting of equation (7) for each impact. The normal extension is expected to depend both on $We$ and on the history of the liquid on the surface prior to reaching the edge [41]. To investigate this latter dependency, the maximum normal extension $l_{nM}$ is shown as a function of the dimensionless offset $\delta$ in figure 9b. A linear decrease of $l_{nM}$ with $\delta$ is observed, that systematically converges to $l_{nM} = 0$ for $\delta = 0.9$. The dependence of the slope of $l_{nM}(\delta)$ on $We$ is approximately:

$$\frac{l_{nM}}{R_0} = 0.36\sqrt{We}(0.9 - \delta) \tag{8}$$

$$\simeq 0.44\frac{V_0 t_c}{R_0}(0.9 - \delta) \tag{9}$$

where the coefficients 0.36 and 0.9 are obtained from best fit. The coefficient 0.9 in equation (8) indicates that $l_{nM} = 0$ for $\delta = 0.9 < 1$. This is counter-intuitive since on the solid, away from the edge, the spreading is slightly larger (by 10%). Spreading continues beyond $R_s/R_{sM} = 0.9$. Corrugations form more quickly in the air around the sheet than when spreading on the solid. Since our measurement of the sheet extension does not include these corrugations, it yields $l_{nM} = 0$ for $\delta = 0.9$.

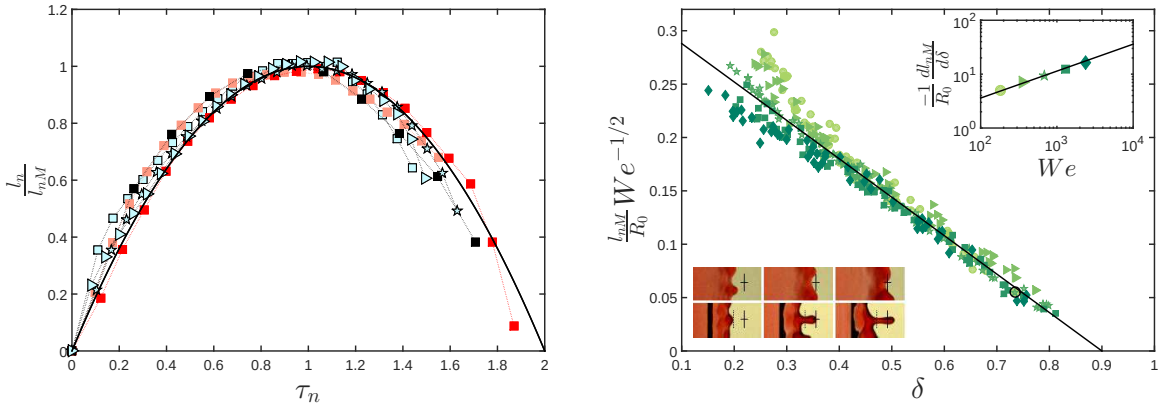


(a) (b)

FIG. 9. (a) Normalized time evolution of the sheet extension normal to the edge $l_n(t)$ for the six examples of figures 4 and 5. The colours represent the different scenarios corresponding to these examples: I (black), II (red) and III (blue). The solid line is (8). (b) Maximum normal extension of the liquid sheet $l_{nM}$ normalised by $R_0 We^{1/2}$ as a function of $\delta$. The solid line shows equation (8), which is fitted on all the data points (with $d/R_0 > 1.3$). Symbols correspond to different $We$ (186 (◯), 367 (▷), 700 (★), 1340 (□), 2435 (♢)).

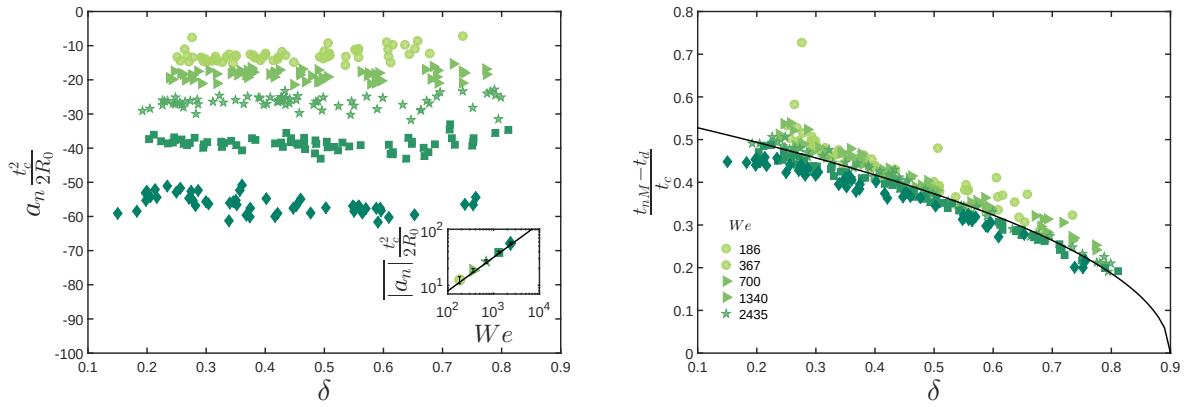


(a) (b)

FIG. 10. (a) Non-dimensional acceleration $a_n$ of the sheet normal to the edge as a function of offset $\delta$. Inset shows the absolute value of $a_n$, averaged over $\delta$, as a function of $We$. The solid line is equation (10). (b) Normalised time of maximum normal extension $(t_{nM} - t_d)/t_c$ as a function of the offset $\delta$. The solid line corresponds to equation (11). Symbols in We: 186 (◯), 367 (▷), 700 (★), 1340 (□), 2435 (♢).

The acceleration of the sheet normal to the edge is obtained by differentiating equation (7) twice: $a_n = -2l_{nM}/(t_{nM} - t_d)^2$. Figure 10a shows that $a_n$, scaled by $t_c^2/(2R_0)$, is remarkably independent of the offset $\delta$. Its average $\overline{a_n}$ over the full range of $\delta$ follows a power law in $We$:

$$\overline{a_n}\frac{t_c^2}{2R_0} = -0.5We^{0.6} \tag{10}$$

where the coefficient 0.5 and the exponent 0.6 are again obtained by fitting experimental data. The exponent close to 0.5 suggests that $\overline{a_n}$ is almost proportional to $V_0/t_c$.

The time $t_{nM}$ needed to reach the maximum extension is deduced from equations (8) and (10). The ratio gives a dependency in $We^{-0.05}$, negligible at first order. In dimensionless form,

$$\frac{t_{nM} - t_d}{t_c} \simeq 0.6\sqrt{0.9 - \delta}. \tag{11}$$

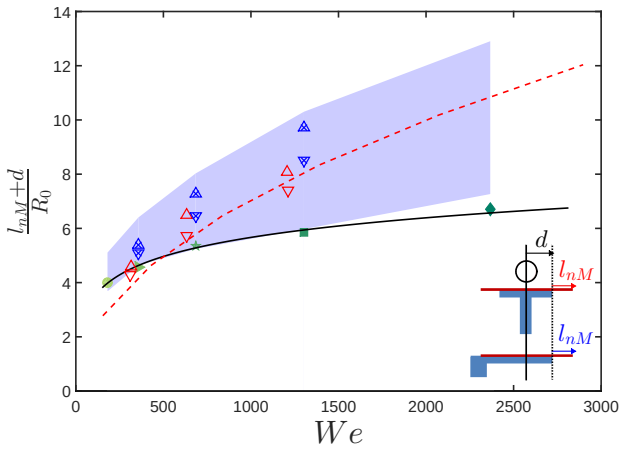


FIG. 11. Comparison of the maximum radial distance from the impact point reached by the liquid for three configurations: full spreading on a solid (filled green symbols), liquid sheet from a flat edge (shaded area), and liquid sheet from a pole (empty triangles). In the first case, the represented variable is $R_{sM}$, while it is $d + l_{nM}$ in the second and third cases. The geometrical similarity of the edge and pole configurations is illustrated with a schematics at the bottom right. Two ratios of pole to drop radius were considered: $d/R_0 = 1.5$ ($\triangle$) and $d/R_0 = 2.4$ ($\triangledown$). The crossed $\triangledown$ and $\triangle$ represent the maximal distance reached in edge experiments with the same offsets $d/R_0$. The solid and dashed lines correspond to equations (3) and (12) respectively.

where 0.6 is obtained using a best fit while ignoring the dependency to $We$. This result compares well with the experimental data (figure 10b). In summary, the kinematics of the sheet extension normal to the edge as a function of $We$ and $\delta$ is well captured by the combination of (7), (9) and (11).

### C. Comparison to the radial extension in axisymmetric impact configurations

The impact near an edge involves the succession of spreading on solid and expansion in the air. It might then be seen as an intermediate configuration between two axisymmetric configurations already investigated: an impact on solid with full spreading [64] and a centred impact on a very small circular target (e.g. the flat tip of a pole) [38]. In order to compare the maximum distance reached by the liquid in these three configurations ($R_{sM}$ on solid, $l_{nM} + d$ on pole and straight edge), we have performed a few additional experiments of impacts on a pole. The pole radius $d$ corresponds to the distance that the liquid must travel on solid before taking off, so it is equivalent to the offset $d$ defined earlier for the impact near an edge. We considered two ratios of pole to drop radius, $d/R_0 \in \{1.5, 2.4\}$ and three Weber numbers $We \in \{370, 700, 1340\}$. For the sake of comparison, the substrate material and the impacting drop (size, composition) are the same as for the edge configuration. Data are reported in figure 11, where they are also compared with several models from previous works: (i) the maximum spreading radius on a solid $R_{sM}$ from Laan *et al.* [64] (3), (ii) the maximum radial extension of the liquid sheet (from impact point) from Rozhkov *et al.* [38], Vernay *et al.* [40]

$$\frac{l_{nM} + d}{R_0} \simeq 0.23\sqrt{We}. \tag{12}$$

The prefactor 0.23 in (12) corresponds to the rounded average between the prefactor 0.227 obtained for $d/R_0 \in \{1, 1.4\}$ by Rozhkov *et al.* [38] and the prefactor 0.22 obtained for $d/R_0 = 1.67$ in Vernay *et al.* [40].

It is confirmed from figure 11 that the liquid sheet for large We and small offsets always goes further than the liquid that only spreads on the solid. Indeed, spreading on the solid generates a lot of energy dissipation through viscous friction, that slows down the liquid spreading. The experimental values of $R_{sM}$ are in good agreement with equation (3). More surprisingly, the maximal distance reached by the liquid sheet is always higher with a straight edge than with a circular edge at the same distance $d/R_0$ from the impact point. This is counterintuitive since in all the directions that are not normal to the straight edge, the liquid has to spread more than $d$ on the solid before taking-off from the edge. By contrast, in the pole configuration, the liquid sheet forms at the same time after the same spreading distance $d$ in every direction. A possible explanation for this larger distance reached by the sheet from a straight edge is that the rupture of symmetry prevents some efficient axisymmetric pulling of the sheet by surface tension.

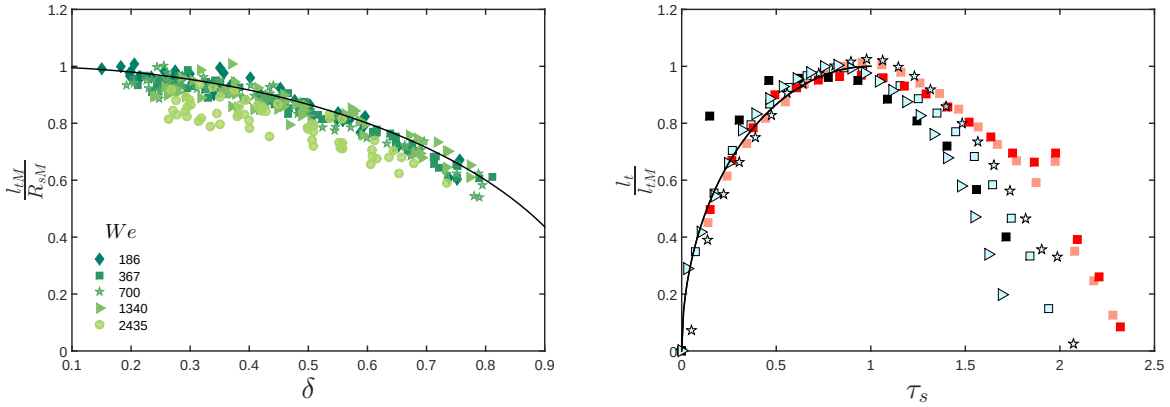


(a) (b)

FIG. 12. (a) Maximum extension $l_{tM}$ of the liquid sheet along the edge normalised by the maximum spreading on solid $R_{sM}$, as a function of the offset $\delta$. The solid line is $\sqrt{1-\delta^2}$, in agreement with (14). (b) Time evolution of the sheet extension along the edge $l_t(t)$, normalised by its maximum value $l_{tM}$ for the six examples of figures 4 and 5. Colours correspond to scenarios: I (black), II (red) and III (blue). The solid line for $\tau_t < 1$ represents (13). Symbols are different $We$: 186 (◯), 367 (▷), 700 (★), 1340 (□), 2435 (♢).

Equation (12) is in good agreement with our experimental data on pole.The power-law $l_{nM} \sim We^{1/2}$ (8) for the edge is similar to the dependence in $\sqrt{We}$ of (12) obtained for the pole [38, 40].

### D. Expansion/retraction of the liquid sheet in the air, along the edge

We proceed by rationalising the time evolution of the liquid sheet in the vicinity of the edge. As seen in figure 2b-d, the extension of the sheet along the edge closely follows the spreading on solid during the expansion phase (By contrast, dewetting on solid is much slower than the retraction of the sheet along the edge). This tangential extension should therefore be geometrically related to the spreading law $R_s(t)$ through $l_t(t) = \sqrt{R_s(t)^2 - d^2}$. Combining this equation with (2) and (5) yields

$$l_t(t) = R_{sM}\sqrt{1-\delta^2}\sqrt{\tau_s(2-\tau_s)}, \text{ with } \tau_s = \frac{t-t_d}{t_{sM}-t_d}. \tag{13}$$

By identification of equations (2) and (13), we would infer that

$$l_{tM} = R_{sM}\sqrt{1-\delta^2}. \tag{14}$$

This prediction is fairly well verified by the experimental measurements of the maximum tangential extension in figure 12a.

In figure 12b, the extension $l_t(t)$ tangent to the edge is represented for the 6 examples of figures 4 and 5, normalised by its maximum value $l_{tM}$ and plotted as a function of $\tau_s$. Thanks to this normalisation, data from these different experiments collapse well onto a single curve during the expansion phase ($\tau_s < 1$) and follow well (13). However, data from different offsets $\delta$ diverge from each other during the retraction phase ($\tau_t > 1$). This scattering of the retraction kinematics along the edge may be linked to the uncontrolled dewetting on this flat vertical edge.

Finally, the time at which the sheet collapses along the edge is defined as $t_r - t_d$. This time is different from the full collapse of the liquid sheet only for the experiments of scenario 3. This collapse time normalized by the time of maximum normal extension is defined as $\tau_r = t_r - t_d/t_{nM} - t_d$ and is illustrated in figure 13. Its value is comprised between 1.3 and 2.1 with an average value across all offsets of 1.76 and a standard deviation of 0.2. Smaller offsets present smaller values and collapse in We. As the offset increases a small separation in We appear although the values end up saturating for large offset where they again collapse.

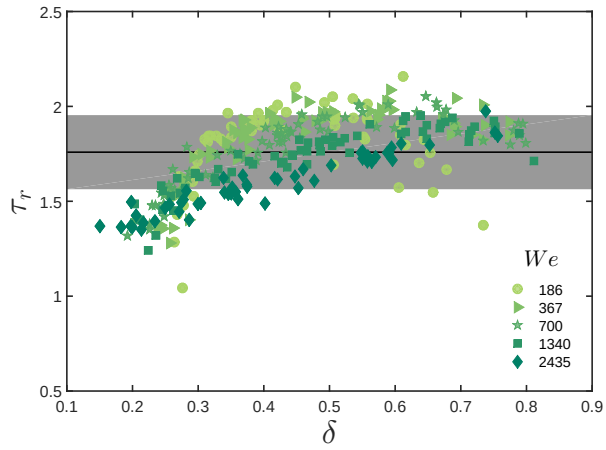


FIG. 13. Normalised time of collapse $\tau_r = t_r - t_d/t_{nM} - t_d$ of the liquid sheet along the edge as a function of the offset $\delta$. Symbols corresponds to $We$ in table I. The solid line is the average across We and $\delta$ and the grey area corresponds to one standard deviation.

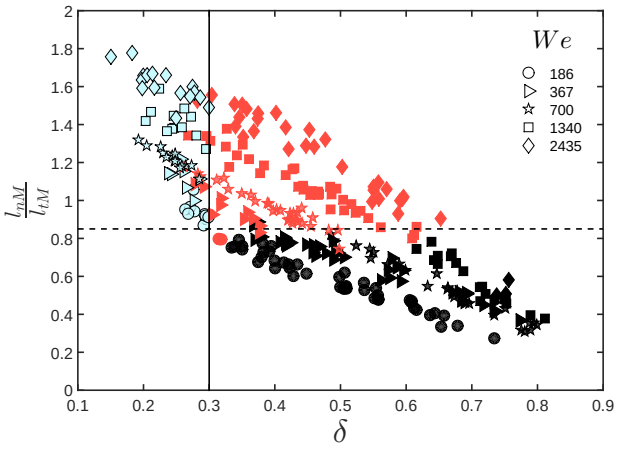


FIG. 14. Scenarios of liquid sheet expansion/retraction, in a $(\delta, l_{nM}/l_{tM})$ diagram. The symbols correspond to different $We$ given in table I and the colours to different scenarios: I (black), II (red) and III (blue). The solid and dashed lines correspond to equations (15) and (16) respectively.

### E. Asymmetry and sheet envelope

In figure 4, we have observed three qualitatively different scenarios of sheet expansion and retraction. Each scenario is observed in a given region of the diagram $(We, d/R_0)$ in figure 6. Boundaries between these regions are non-trivial in this diagram. The preceding investigation of the sheet kinematics highlighted the importance of the dimensionless offset $\delta = d/R_{sM}$. Moreover, a key difference between the scenarios is the relative asymmetry of the sheet, which could be represented by the ratio $l_{nM}/l_{tM}$. The separation of scenarios appears more clearly in the diagram $(\delta, l_{nM}/l_{tM})$ of figure 14. With this representation, the transition from scenarios (III) to (II) occurs approximately at

$$\delta = 0.3, \tag{15}$$

and the transition from scenarios (I) to (II) at

$$\frac{l_{nM}}{l_{tM}} = 0.85. \tag{16}$$

The distance travelled by the liquid spreading on the solid strongly influences the subsequent shape of the liquid sheet in the air. Based on this observation, we propose a first-order model to reconstruct the maximal region accessible

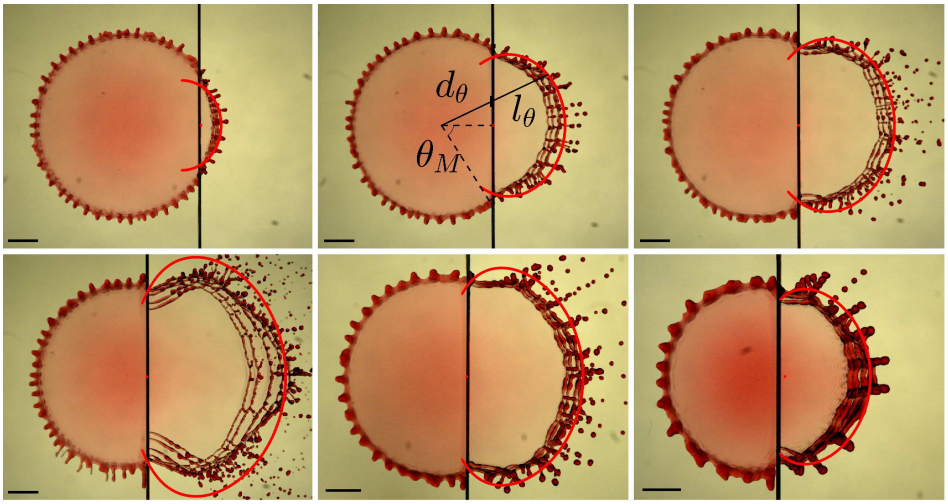


FIG. 15. Time superposition of snapshots from a given experiment, with $t \in [t_{tM}, t_{nM}]$. The red line represents the reconstructed envelope region accessible to the sheet, predicted from (17). (Top line) From left to right, $We = 1300$ and $\delta = 0.79$, 0.54, 0.34. (Bottom line) From left to right, $We = 1300$, 350 and $d/R_0 = 1.3$, with $\delta = 0.22$, 0.24, 0.28. Scale bars are 4 mm.

to the expanding sheet. On the solid, the liquid spreads radially from the impact point and reaches the edge after a distance $d_\theta = d/\cos\theta$, where $\theta$ is the angular position from the impact point, measured from the symmetry axis (figures 7 and 15). Since $d_\theta$ is bounded by $R_{sM}$, $\theta$ must be smaller than $\theta_M = \cos^{-1}\delta$. By replacing $d$ by $d_\theta$ (or equivalently $\delta$ by $\delta/\cos\theta$) in equation (8), we obtain a prediction of the maximum extension $l_\theta$ reached by the sheet in direction $\theta$:

$$\frac{l_\theta}{R_0} = 0.36We^{1/2}\left(0.9 - \frac{\delta}{\cos\theta}\right). \tag{17}$$

Since the time of maximum extension varies with the direction considered (i.e. $t_{nM} \neq t_{sM} - t_d$), equation (17) does not predict the shape of the sheet at a given instant. It rather gives the envelope region accessible to the sheet during its expansion. This reconstruction is illustrated in figure 15 for various $We$ and $\delta$. In most of the cases, the prediction (17) captures well the sheet envelope. It only strongly overestimates that envelope for the largest $We$ and smallest $d$ (bottom left picture in figure 15) that corresponds to the third scenario. In that particular case, the time of the maximum normal to the edge occurs much later than the tangential one. The antagonist movements between the tangential retraction and the normal extension might explain the difference in the experimental vs. theoretical envelope of the sheet.

## V. DROPLET EJECTION

In this section, we characterise the ejected droplets from a statistical point of view, and we relate their properties to the asymmetric kinematics of the sheet. We successively discuss the mechanisms and direction of ejection, the initial speed, the number and the mass and the travelled distance of ejected droplets. More details on droplet tracking and mass estimation are provided in appendix 1.

### A. Ejection mechanisms and direction of ejection

Three ejection mechanisms are identified and illustrated in figure 16. They are differentiated according to the time, position, and directionality of the ejections (figure 17). Their speed and ejection time are highlighted in figure 18. The selected snapshots correspond to parts of the movies illustrated in figure 4.

- The first mechanism is called radial ejection (figure 16 - top left). It concerns droplets from the rim of the sheet (i.e. before sheet collapse), for which the ejection direction $\theta_v$ is closely aligned on the radial position from the impact point $\theta_x$ (definition in figure 7). Each droplet originates from a corrugation along the rim. This corrugation grows in a radial filament (almost normal to the sheet) by inertia, owing to the constant deceleration of the

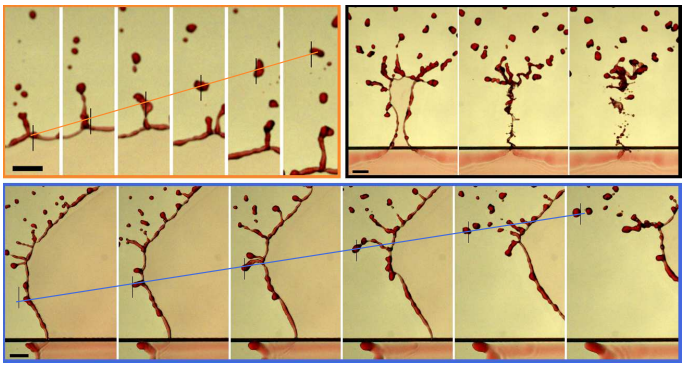

FIG. 16. Mechanisms of droplet ejection: (top left) Radial ejection from the rim. Successive snapshots are separated by 0.4 ms, from 6.2 ms after impact. The highlighted droplet is ejected at $\tau_n = 1.02$, with a mass $m = 0.23$ mg and a speed $v = 0.28V_0$. Its ejection angles are $\theta_x = 4°$ and $\theta_v = -9°$. (bottom) Tangential ejection from the rim. Successive snapshots are separated by 0.6 ms, from 4 ms after impact. The highlighted droplet is ejected at $\tau_n = 1.17$, with a mass $m$= 0.29 mg and a speed $v$ = 0.46 $V_0$. Its ejection angles are $\theta_x = 48°$ and $\theta_v = 7°$. (top right) Collapse of the sheet. Snapshots are taken at 11.8 ms, 12.2 ms and 13 ms after impact. The three scale bars are 2 mm. The orange and blue solid lines join the centre of mass of the ejected droplets across frames. The vertical black lines are at fixed position, so they highlight the left-to-right motion of the droplets. These three snapshots correspond to zooms on the droplet ejections framed in figure 4.

sheet. The filament then destabilises into one or several droplets that are ejected perpendicularly to the rim. The droplets mostly inherit the normal velocity that the sheet had during the early growth of the corrugations. They also inherit a small velocity tangent to the rim, that corresponds to a slight lateral displacement of the corrugation.

- The second mechanism is called tangential ejection (figure 16 - bottom) and it again concerns droplets ejected from the rim of the sheet. In this case, the ejection direction $\theta_v$ is not aligned anymore on the radial position $\theta_x$. This mechanism mostly appears on the sides of the sheet in the most asymmetric scenarios, i.e. (II) and (III). Owing to inertia, the corrugations in which liquid accumulates travel along the rim, away from the edge. When the rim retracts tangentially to the edge, these corrugations destabilise into droplets. However, the velocity inherited by the droplets now mostly comes from the motion of the corrugations along the rim, and not anymore from the velocity of the sheet. Consequently, these droplets are ejected in a direction almost parallel to the rim, and perpendicular to its retraction velocity. As the capillary force from the sheet does not directly oppose the motion of these corrugations, the resulting droplets tend to go faster than the droplets ejected radially. This is illustrated in figure 16.

- The last mechanism occurs when the sheet collapses (figure 16 - top right). The resulting liquid filament has a very complex shape and it breaks up in a wide variety of droplets. These droplets may inherit from the late retraction speed of the sheet. A particular collapse event is present when the sheet retracts in scenarios (II) and (III). The two rims of the sheet near the edge converge quickly towards each other. Their violent collision generates many droplets that are much smaller than those emitted from the two first mechanisms. The direction of ejection can also be out of the plane of the sheet (figure 2g-h).

The prevalence of each ejection mechanism is observed in figure 17, where the direction $\theta_v$ of droplet ejections is plotted against their angular position $\theta_x$. Droplets are distinguished according to the sheet kinematics (expansion, retraction, collapse) at the moment of their ejection. During sheet expansion ($\tau_n < 1$), most droplets are ejected radially, i.e. with $\theta_v \simeq \theta_x$. Tangential ejections only appear during sheet retraction ($1 < \tau_n < \tau_r$), when the sheet asymmetry is sufficiently developed. SOPHIE, WE NEED TO INTRODUCE $\tau_r$ SOMEWHERE IN THE SHEET DESCRIPTION... At small offset $\delta$, most of them satisfy $|\theta_v| < |\theta_x|$, so their ejection direction is more normal to the edge than a droplet ejected radially from the same position. At large $\delta$, the direction of tangential ejections is much more scattered. Droplets ejected from the collapse of the sheet ($\tau_n > \tau_r$) remain localised close to the symmetry axis, in $|\theta_x| \lesssim 20°$. However, their ejection direction $\theta_v$ is much more scattered than for other mechanisms.

The radial ejection mechanism was already observed in the axisymmetric configuration of impact on a pole [39], and the mass distribution was characterised. The collapse mechanism is also observed in such impacts when the sheet experiences local piercing - this typically occurs when the impact is not perfectly centred on the pole. The tangential ejection mechanism and the filament breakup are not present in the axisymmetric impact configuration.

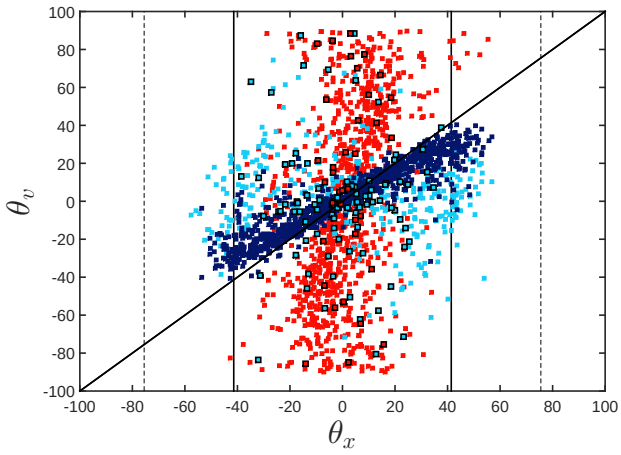


FIG. 17. Angle of the ejection velocity $\theta_v$ as a function of the angular position of ejection $\theta_x$ measured from the impact point (defined in figure 7), for $We = 1300$. Symbols without black contour (resp. with black contour) correspond to $\delta \in [0.2, 0.3]$ (resp. $\delta \in [0.7, 0.8]$). The colour refers to the ejection time: (dark blue) during sheet expansion, i.e. $\tau_n < 1$, (light blue) during sheet retraction, i.e. $1 < \tau_n < \tau_r$, and (red) after sheet collapse, i.e. $\tau_n > \tau_r$. The inclined solid line is the bisector $\theta_v = \theta_x$. The vertical lines correspond to the maximum sheet angle $\theta_M$ (defined in figure 15), for $\delta = 0.25$ (dotted) and $\delta = 0.75$ (solid).

### B. Droplet ejection speed

The speed $v$ at which each droplet is ejected is represented as a function of its ejection time in figure 18, for the six examples of figures 4 and 5. The speed $v$ is naturally normalised by the impact speed $V_0$, while the time $\tau_n$ is normalised by the time of maximum extension of the sheet normal to the edge. All the data corresponding to normal extension ($\tau_n < 1$) collapse on to a single curve, so $v/V_0$ is a decreasing function of $\tau_n$ only, for all $We$ and $\delta$. The ejection speed becomes more scattered as soon as $\tau_n > 1$, i.e. during the retraction and collapse of the sheet. The time of full retraction of the sheet along the edge is denoted $\tau_r$. This time is equivalent to the full collapse or pinch of the sheet along the edge. It here corresponds to a maximum scatter of the ejection speed.

The influence of the sheet kinematics on droplet ejection can be better assessed by looking at the speed of the sheet in the direction normal to the edge (derived from (7)):

$$\frac{1}{V_0}\frac{dl_n}{dt} = \frac{2l_{nM}}{V_0(t_{nM} - t_d)}(1 - \tau_n) \simeq 1.47\sqrt{0.9 - \delta}(1 - \tau_n) \tag{18}$$

The normal extension speed of the sheet is again proportional to the impact speed $V_0$ in first approximation. It is reported in figure 18, where it sets a lower limit to the droplet ejection speed. Indeed, ejected droplets during the sheet expansion must always go faster than the sheet from which they detach. It confirms that the ejection speed $v$ is strongly inherited from the sheet kinematics.

A careful examination of figure 18 indicates that, for $\tau_n > 1$, the scattering of ejection speed at a given time depends on the considered scenario. Data from scenario (I) align in the continuity of the curve observed for $\tau_n < 1$, without much scattering. The corresponding droplets are radially ejected, through the same mechanism as all the droplets ejected in $\tau_n < 1$. By contrast, the ejection speed at $\tau_n > 1$ is much more scattered for scenario (II) and (III), which suggests the emergence of tangential ejections. In order to better quantify this scattering, we define a theoretical ejection speed $v_T(\tau_n)$ that corresponds to the average speed of all the droplets radially ejected at a given $\tau_n$. These considered droplets are from all scenarios together when $\tau_n < 1$, and only from scenario (I) when $\tau_n > 1$. This theoretical velocity is well approximated by an exponential decrease:

$$\frac{v_T}{V_0} = 2.1e^{-2.5\tau_n} + 0.1 \tag{19}$$

where coefficients 2.1, 2.5 and 0.1 are the best fitting parameters (figure 18).

Deviations from this theoretical speed $v_T$ of radial ejections can be first calculated in terms of an average over all the data from a given scenario. This pooling of offsets per scenario is denoted with an overline followed by an exponent $s$. The evolution of $\overline{v/v_T}^s$ and its corresponding standard deviation are represented in figure 19 (middle). When $\tau_n < 1$, the average value is close to 1 for all scenarios, which is expected from the definition of $v_T$. The

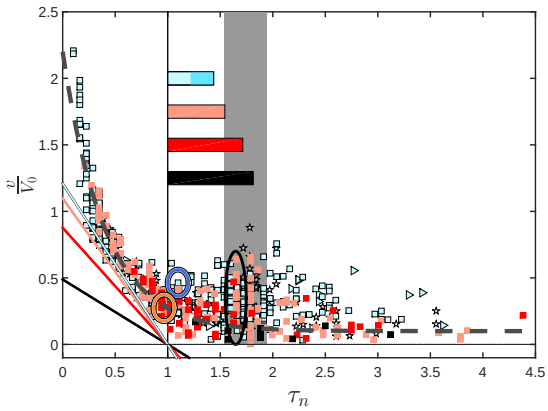


FIG. 18. (Colour online) Time evolution of the droplet ejection speed $v$ (normalised by the impact speed $V_0$) for the six examples of figures 4 and 5. The time $\tau_n$ is normalised according to the normal extension of the sheet. Each data point corresponds to a single droplet. Symbols correspond to Weber number, $We = 350$ (▷), 680(★), 1300(□), while colours indicate asymmetry from least (I) to most (III) with I (black), II (red) and III (blue). Horizontal rectangles represent the duration of the sheet retraction. The darker blue rectangle in scenario III corresponds to the retraction of the sheet after it has pinched from the edge. The grey area indicates the time $\tau_r$ at which the sheet has fully retracted from the edge (average across $We$ and $\delta$, plus/minus standard deviation). The inclined solid lines correspond to (18) for the six examples (one line per scenario). The dotted line represents (19). Circled data points correspond to the snapshots of figure 16.

standard deviation is an order of magnitude smaller, which confirms the good collapse of the data already seen for $\tau_n < 1$ in figure 18. As soon as $\tau_n \gtrsim 1$, both the average and the standard deviation increase for scenarios (II) and (III), which corresponds to the appearance of tangential droplets. This increase is sharper as the scenario describes a more asymmetric behaviour. A maximum is observed around the time of full retraction from the edge $\tau_r$, beyond which the average and standard deviation decrease. The average for scenario (I) remains close to 1 for $\tau_n > 1$, which confirms that the theoretical prediction $v_T$ can indeed include the droplets from scenario (I) ejected radially during the retraction of the sheet.

Variations of the ejection speed with $We$ and $\delta$ are studied by calculating averages (and corresponding standard deviations) over specific time intervals for all experiments at given $(We, \delta)$. These averages are defined for any variable $x$ :

$$\begin{aligned}
\langle x\rangle^1 &: \quad \text{average over sheet expansion,} && \tau_n < 1 \\
\langle x\rangle^2 &: \quad \text{average over sheet retraction,} && 1 < \tau_n < \tau_r \\
\langle x\rangle^3 &: \text{average after full sheet retraction from the edge,} && \tau_n > \tau_r \\
\langle x\rangle^{2-3} &: \quad \text{average after sheet expansion,} && \tau_n > 1, \\
\langle x\rangle &: \quad \text{average over all time} && \tau_n > 0.
\end{aligned} \tag{20}$$

As seen in figure 19 (left), the average speed during sheet expansion is again very close to the theoretical speed of radially-ejected droplets, i.e. $\langle v/v_T\rangle^1 \sim 1$, for all $We$ and $\delta$. The corresponding standard deviation is about seven times smaller. Furthermore, the Probability Distribution Function $PDF\left(\langle v/v_T\rangle^1\right)$, that includes all droplets ejected for $\tau_n < 1$, follows a Gaussian distribution of mean 1.05 and standard deviation 0.2 (figure 19-inset). During the retraction and collapse of the sheet, both the average of $\langle v/v_T\rangle^{2\text{-}3}$ and the corresponding standard deviation decrease linearly with $\delta$, as seen in figure 19 (right). There is almost no dependence to $We$, which indicates that the sheet asymmetry (measured by $\delta$) pilots the droplet ejection pattern during the sheet retraction and collapse.

### C. Droplets numbers and masses

The Cumulative Distribution Function (CDF) of the normalised time $\tau_n$ at which droplets are ejected, i.e. the number of droplets ejected before a given $\tau_n$, is represented in figure 20a for the 6 examples of figures 4 and 5. The number of droplets increases with $We$ and decreases with increasing $\delta$. For all scenarios, the ejection rate (slope of the CDF) remains steady during sheet extension, then it strongly decreases during retraction. In scenarios (II) and (III), there is an additional outburst of droplets at the moment of collapse $\tau_r$, which corresponds to the filament breakup mechanism. The ejection rate decreases again for larger $\tau_n$. For scenarios (II) and (III), the first ejections occur

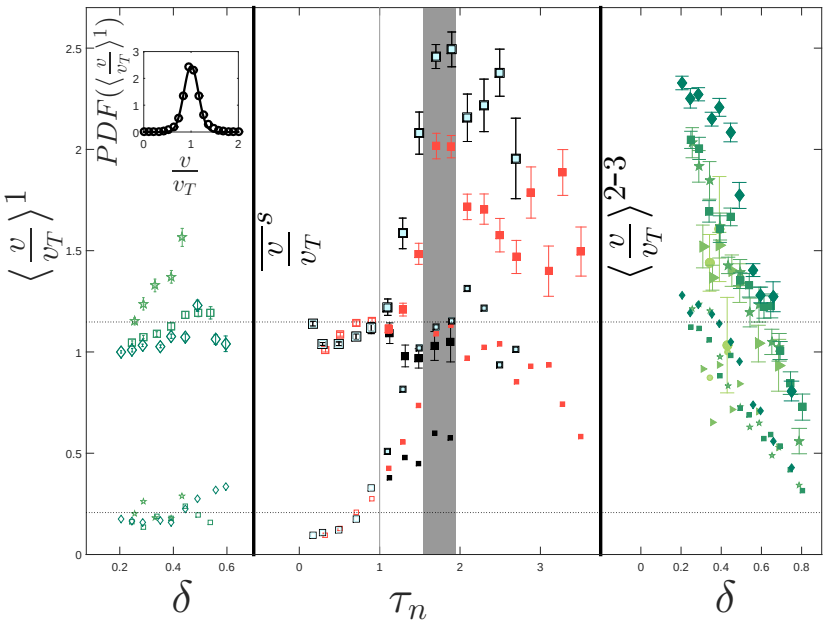


FIG. 19. (Colour online) Average (large symbols) and standard deviation (small symbols) of $v/v_T$. The dotted line is the average over all $(We, \delta)$. (Left) Average over the sheet expansion ($\tau_n < 1$), for each $(We, \delta)$. (Middle) Average over each scenario for $We = 1300$. Colours refer to scenarios: I (black), II (red) and III (blue). The grey area indicates the time $\tau_r$ at which the sheet has fully retracted from the edge (average across $We$ and $\delta$, plus/minus standard deviation). (Right) Average after sheet expansion ($\tau_n > 1$), for each $(We, \delta)$. Inset: PDF of $v/v_T$ during the sheet expansion. The solid line is a fit with a Gaussian distribution of mean 1.05 and standard deviation 0.2. Symbols in We = 180 (◯), 350(▷), 680(★), 1300(□), 2600 (♢).

during the expansion of the sheet. Conversely, in the isotropic scenario (I), ejections only start during the retraction of the sheet.

The average number $N$ of ejected droplets per impact is represented in figure 20b, where data from all experiments have been again pooled by $We$ and $\delta$. This number of droplets increases with $We$, and it decreases almost quadratically with increasing offset $\delta$, among others since the fraction of the impacting drop that crosses the edge decreases. The number of droplets vanishes in $\delta = 0.9$, which also corresponds to a vanishing liquid sheet (equation 8). As confirmed in figure 20b, it can be approximated by

$$N = 0.02We^{1.4}(0.9 - \delta)^2 \tag{21}$$

The mass $m$ of the ejected droplets is reported as a function of their normalised ejection time $\tau_n$ in figure 21a, for the six examples of figures 4 and 5. Contrary to the ejection speed $v$, the mass $m$ varies on more than three orders of magnitude and it is scattered at all time. Nevertheless, $m$ is clearly bounded by a maximal mass that increases with time for $\tau_n < 1$ and saturates to a constant value for $\tau_n > 1$. This maximal droplet mass is still 50 times smaller than the mass $M_0 = 4\pi\rho R_0^3/3$ of the impacting drop. Viscosity sets a lower bound to the size of ejected droplets. In the context of partial coalescence, the inhibition of inertial liquid break-up by viscosity was observed for Ohnesorge numbers $Oh \gtrsim 0.025$ [66, 67]. It here corresponds to a minimum radius of 0.02 mm, and a mass $m/M_0 \simeq 5 \times 10^{-7}$. This size is slightly below the resolution of our camera.

The increase of this upper bound on mass during sheet expansion ($\tau_n < 1$) satisfies a power law

$$\frac{m}{M_0} \leq 0.013\tau_n^{5/2}, \tag{22}$$

that is valid for each scenario so it is presumably independent of the offset $\delta$. Equation 22 suggests to analyse the statistical distribution of droplet mass, normalised by $\tau_n^{5/2}$ (figure 21b). This distribution is now calculated on all data, and not only on the six examples of figure 21a. Data are pooled per $We$ (all $\delta$ together), which is denoted with

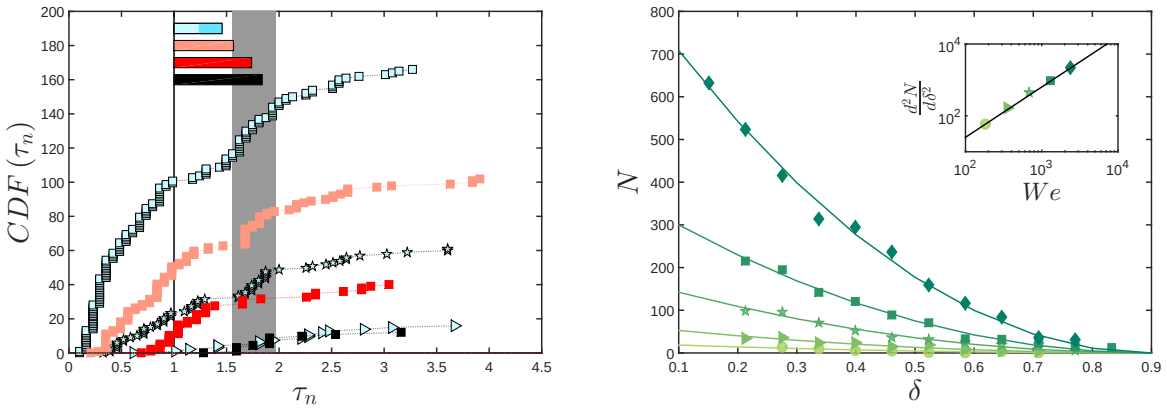


(a) (b)

FIG. 20. (Colour online) (a) Non-normalised Cumulative Distribution Function (CDF, expressed in number of ejected droplets) of the normalised time $\tau_n$ for the six examples of figure 4 and 5. Symbols correspond to Weber number, $We = 350$ (▷), 680(★), 1300(□), while colours indicate scenario, I (black), II (red) and III (blue). The grey area indicates the time $\tau_r$ at which the sheet has fully retracted from the edge (average across $We$ and $\delta$, plus/minus standard deviation). (b) Average number $N$ of droplets ejected per impact, as a function of $\delta$. Symbols in We = 180 (◯), 350(▷), 680(★), 1300(□), 2600 (◇). Solid lines are (21). (Inset) Second derivative of $N$ with respect to $\delta$, as a function of $We$. The solid line corresponds to $\frac{d^2N}{d\delta^2} = 0.04We^{1.4}$ in equation (21).

| Phase | Time | Power law | |
|---|---|---|---|
| Expansion | $\tau_n < 1$ | $\Phi\left(\frac{m}{M_0}\right) \simeq 0.013\tau_n^{5/2}$ | (23) |
| Retraction | $1 < \tau_n < \tau_r$ | $\Phi\left(\overline{\langle\frac{m}{M_0}\rangle^2}\right) = 2.9We^{-3/4}$ | (24) |
| After collapse | $\tau_n > \tau_r$ | $\Phi\left(\overline{\langle\frac{m}{M_0}\rangle^{2\text{-}3}}^{II\text{-}III}\right) = 10^4We^{-1.7}$ | (25) |

TABLE II. Power laws of mass saturations according to the different sheet phases.

a simple overline. The Probability Distribution Function

$$PDF\left(\overline{\langle\frac{m}{M_0\tau_n^{5/2}}\rangle^1}\right)$$

presents a mode that approximately varies as $We^{-0.2}$, so faster incoming drops generate smaller ejected droplets. There is indeed a cut-off on the right end of this PDF, which corresponds to the maximal mass.

We define the maximal value of any variable $X$ as the cut-off $\Phi(X)$ of its statistical distribution. This cut-off is here obtained by approximating the tail of the corresponding Cumulative Distribution Function (CDF) of $X$ with a quadratic function that reaches a maximum of 1 in $\Phi$. The least-square fit is performed with data from quantiles 0.85 to 0.995.

The cut-off mass at $\tau_n < 1$ is determined for each $\delta$ and $We$ independently (figure 21b-inset). It is remarkably independent of $\delta$ and $We$, and its average value is given by (23) from which (22) is derived. Again, once this cut-off mass is expressed as a function of the sheet time $\tau_n$, the explicit dependence to $We$ and $\delta$ disappears, which is characteristic of the droplets radially ejected during the sheet expansion.

During retraction, the mass distribution is almost independent of $\delta$, and it is slightly shifted to lower mass with increasing $We$. By contrast, the distribution after collapse does depend on both $\delta$ and $We$. The cut-off $\Phi$ of the mass distribution of ejected droplets is again calculated separately for each $We$ and $\delta$, first during sheet retraction (figure 22a) and second after sheet collapse (figure 22b). During retraction, the variation of $\Phi\left(\langle m/M_0\rangle^2\right)$ with $\delta$ is very small. Consequently, data from different $\delta$ can be pooled, which reveals a power-law dependence in $We$ (figure 22a - inset) given by (24.

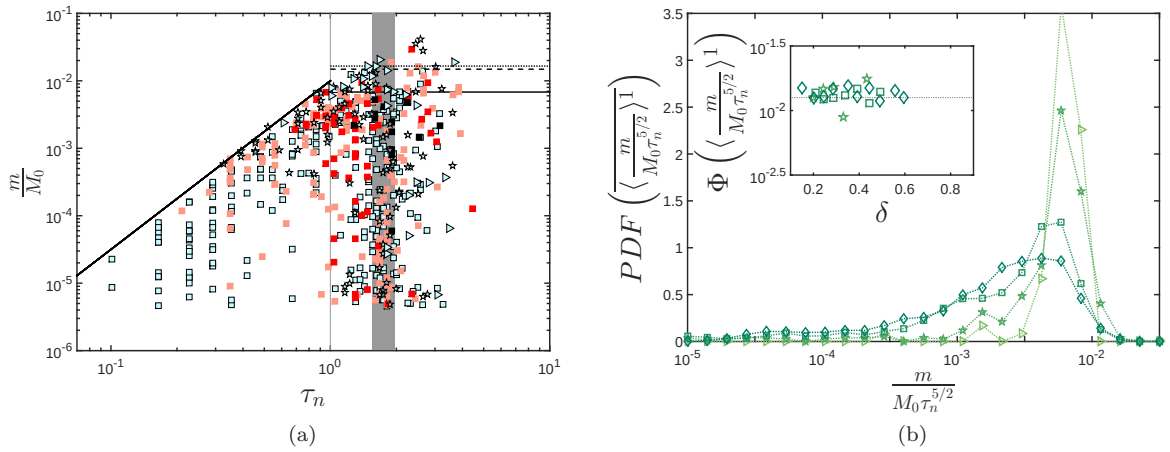


FIG. 21. (Colour online) (a) Time evolution of the mass $m$ of the ejected droplets (normalised by the mass $M_0$ of the impacting drop) as a function of their normalised time of ejection $\tau_n$, for the six examples of figure 4 and 5. Each data point corresponds to a single droplet. Symbols correspond to Weber number, $We = 350$ (▷), 680 (★), 1300 (□), while colours indicate scenario, I (black), II (red), III (blue). The grey area indicates the time $\tau_r$ at which the sheet has fully retracted from the edge (average across $We$ and $\delta$, plus/minus standard deviation). The inclined solid line represents (22). The horizontal lines correspond to (24), with $We = 350$ (dotted), $We = 680$ (dashed) and $We = 1300$ (solid). (b) Probability Distribution Function (PDF) of the normalised mass $m/({M_0}{\tau_n}^{5/2})$ of droplets ejected during sheet expansion ($\tau_n < 1$), pooled per $We$ (all $\delta$ together). The symbols correspond to different $We = 180$ (◯), 350(▷), 680(★), 1300(□), 2600 (♢). Inset: Saturation value $\Phi$ of the PDF, for each $We$ and $\delta$. The dotted line corresponds to equation (23).

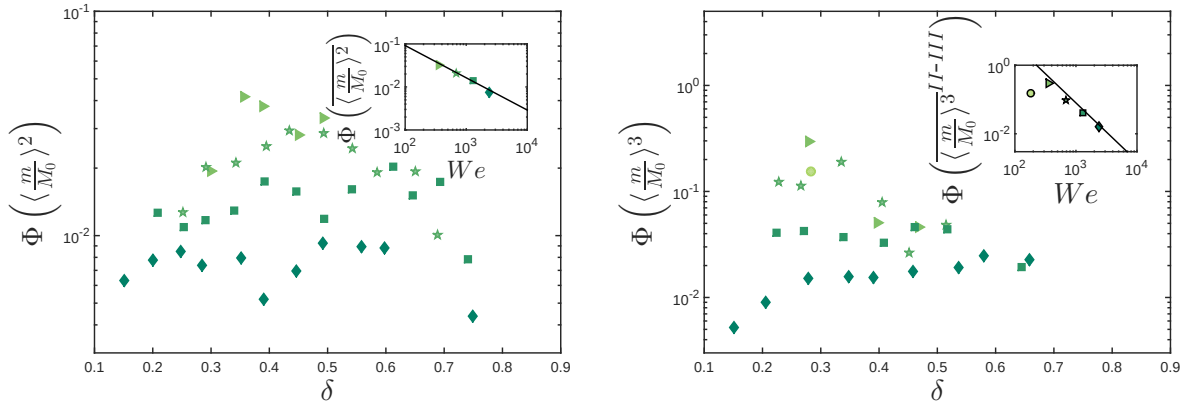


FIG. 22. Cut-off $\Phi$ of the mass distribution of ejected droplets, pooled per $We$ and $\delta$: (a) during the retraction of the sheet, and (b) after collapse of the sheet. Symbols correspond to different $We = 180$ (◯), 350(▷), 680(★), 1300(□), 2600 (♢). Insets: Dependence to $We$ of the cut-off $\Phi$: (a) after pooling all $\delta$. The solid line is equation (24). (b) after pooling scenarios (II) and (III). The solid line is equation (25).

After the collapse of the sheet, $\Phi\left(\langle m/M_0\rangle^3\right)$ is almost independent of $\delta$ at high $We$, but it sharply decreases with increasing $\delta$ at lower $We$. The pooling of scenarios (II) and (III) reveals a decrease of the average cut-off with increasing $We$ given by (25. The comparison of equations (24) and (25) reveals that, for $We \lesssim 4000$, the mass cut-off is larger after collapse than during retraction of the sheet. This fact could be the consequence of (i) the likely merging of ejected droplets after collapse, and (ii) the presence of a very large liquid filament detached from the edge (e.g. in scenario III) that does not instantly destabilise into smaller droplets

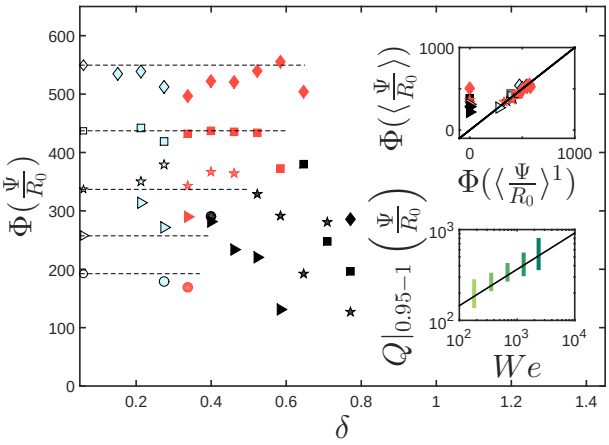


FIG. 23. Maximum horizontal distance $\Phi(\Psi)$ travelled by the ejected droplets, pooled together per $We$ and $\delta$. Symbols correspond to different $We$ (table I) while colours indicate scenario, I (black), II (red) and III (blue). The dashed lines correspond to (26). Top inset: $\Phi(\Psi)$ during the sheet lifetime compared to the one dictated by the droplets ejected during the sheet extension. The solid line is the bisector. Bottom inset: Maximum horizontal distance reached by the droplets as a function of $We$. The thick vertical lines correspond to the range of distance covered by the 5% of droplets that travel the farther (based on experimental mass ejection speed), pooled per $We$. Symbols correspond to different $We = 180$ (◯), 350(▷), 680(★), 1300(□), 2600 (♢). The solid line represents (26).

### D. Distance travelled by the droplets

The ballistic trajectory $\mathbf{x}(t) = x(t)\mathbf{e}_x + z(t)\mathbf{e}_z$ of each ejected droplet can be computed from Newton's law, as a function of its mass $m$ and ejection speed $v$ (Appendix A). We here consider the horizontal direction of ejection, and compute $x(t)$, the distance travelled horizontally since ejection, no matter in which direction $\theta_v$. Owing to air drag, the horizontal speed decreases with time and $x(t)$ reaches an asymptotic value $\Psi = \lim_{t\to\infty} x$ called the aerodynamic wall [68].

The cut-off $\Phi(\Psi)$ of the statistical distribution of $\Psi$ is calculated by pooling all ejected droplets from different experiments at given $We$ and $\delta$ (figure 23). When the offset $\delta$ is in the range of scenarios (II) and (III), $\Phi(\Psi)$ is fairly independent on $\delta$. By contrast, when $\delta$ is in the range of scenario (I), $\Phi(\Psi)$ decreases with increasing $\delta$. The similarity of $\Phi(\langle\Psi\rangle)$ and $\Phi(\langle\Psi\rangle^1)$, illustrated in the parity plot of figure 23-top inset, suggests that the cut-off distance $\Phi(\Psi)$ is already reached by the droplets ejected during the sheet expansion ($\tau_n < 1$), if any (i.e. for scenarios (II) and (III)). Droplets ejected afterwards ($\tau_n > 1$) can travel as far, but not significantly farther. The upper bound of $\Psi$ first increases with time, until a maximum value $\Psi_M$ is reached slightly before $\tau_n = 1$. This maximum $\Psi_M$ during expansion can be predicted from the maximal mass $\Phi\,(m/M_0)$ given by equation (23), and the quantile 90% of the ejection speed. During sheet expansion, the speed distribution is approximately normal with mean $v_T$ and standard deviation $0.2v_T$ (figure 19), so this quantile is estimated as $Q_{90}\,(v_T/V_0) = \left(1 + 0.2\sqrt{2}\mathrm{erf}^{-1}(0.8)\right)(v_T/V_0) = 1.26v_T/V_0$. Since both mass and speed bounds are independent of $\delta$ during sheet expansion (figures 19-left and 21b-inset), $\Psi_M$ is also independent of $\delta$. Droplets of scenario (I) are only ejected in $\tau_n > 1$, when the average speed is already low (figure 19-middle) while the mass is not necessarily larger (figure 22a). As a result, droplets from scenario (I) travel much less far than those of other scenarios.

It can be shown numerically that, for the range of $We$ considered in this study, $\Psi_M$ is approximately given by

$$\frac{\Psi_M}{R_0} \simeq 23We^{2/5}. \tag{26}$$

This prediction of the maximal distance reached by droplets is compared to the distance $\Phi(\Psi)$ calculated from droplet mass and speed measured experimentally. All ejected droplets are pooled per $We$ and only the intervall covered by the furthest-going 5% is considered (figure 23-bottom inset). Equation 26 provides a practical first-order approximation of the distance that ejected droplets can possibly reach at a given $We$.

This upper bound on travelled distance, originally derived from droplets ejected during sheet expansion, seems to hold for droplets ejected when the sheet retracts and collapses. However, droplets from these two latter phases can be up to ten times heavier than those from the expansion, even those which travel as far. This is illustrated for two

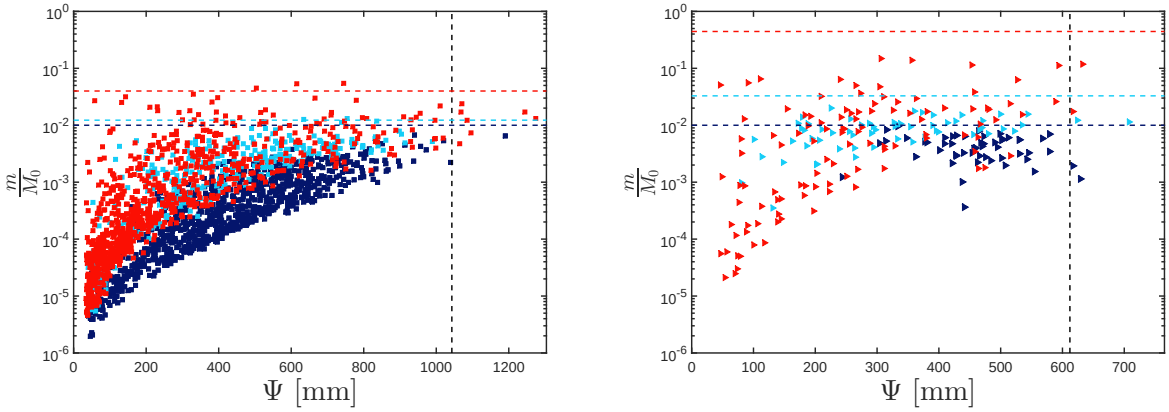


FIG. 24. Mass $m$ of the ejected droplets as a function of their travelled distance $\Psi$. (a) $We = 350$ (▷). (b) $We = 1300$ (□). In both (a-b), $\delta \in [0.2 - 0.3]$. The colour indicates the ejection time: during sheet expansion ($\tau_n < 1$, dark blue), during sheet retraction ($1 < \tau_n < \tau_r$, light blue) and after sheet collapse ($\tau_n > \tau_r$, red). The vertical dotted line represents the (26). The horizontal dotted lines in dark blue, light blue and red correspond to (22) (evaluated in $\tau_n = 1$), (24) and (25), respectively.

different $We$ in the $(\Psi, m)$ diagrams of figure 24b. Tangentially-ejected droplets are often among these outperforming droplets, since they inherit from a mass similar to the radially-ejected droplets, with a possibly larger speed.

## VI. DISCUSSION - CONCLUSION

There are many different configurations in which raindrops can impact on plant leaves and subsequently fragment into droplets. Some of these configurations are particularly efficient at ejecting these droplets far away. They are consequently of primary relevance for the dispersal of pathogens initially present on infected leaves. A common feature observed in most impact configurations is the formation and break-up of an asymmetric liquid sheet, connected to the substrate on one side, and delimited by a rim entirely in the air on the other side. In this paper, we have investigated the impact of a drop at speed $V_0$ next to the straight edge of a flat horizontal substrate. A similar sheet is formed and fragmented, but the kinematics is much easier to visualise and quantify since both the sheet and the ejected droplets move approximately in the plane of the substrate. Moreover, this configuration involves only two relevant dimensionless parameters: the offset $d$ and the Weber number $We$. We have varied both parameters, with the latter in a range similar to that of raindrops. From video recordings, we have systematically tracked and quantified the motion of both the sheet and the ejected droplets.

The evolution of the sheet in the direction normal to the edge is approximately symmetric in time. It is advantageously described by measuring the time from its birth, at the instant $t_d$ at which the liquid takes-off from the substrate. The duration of the sheet extension $t_{nM} - t_d$ is then approximately proportional to the capillary time $t_c$ (equation 11), with a corrective factor that mostly depends on the ratio $\delta$ between the offset $d$ and the maximum spreading distance on the solid $R_{sM}$. The maximum extension $l_{nM}$ of the sheet normal to the edge is approximately proportional to $V_0 t_c$ (equation 9), with again a corrective factor to take the initial spreading on solid into account. This latter is linearly decreasing with $\delta$. Remarkably, the corresponding acceleration, which then scales as $V_0/t_c$, is constant in time and does not depend on $\delta$ anymore. We have also shown that, against intuition, the sheet can extend farther from the substrate when a drop impacts at a distance $d$ from a flat edge than when it impacts at the centre of a pole of radius $d$.

The evolution of the sheet along the edge is not symmetric in time. Its extension follows the adjacent spreading on the substrate, while its retraction involves some dewetting of the edge. The important scatter of the corresponding data suggests the presence of uncontrolled contact line pinning during this retraction phase. The asymmetry of the sheet shape strongly depends on $\delta$. We identified three different scenarios, that correspond to characteristic shapes of the sheet. The boundaries between these scenarios can be rationalised by considering the competition of sheet kinematics in directions normal and tangent to the edge.

Ejected droplets were characterised statistically in terms of number, mass, speed, direction and time of ejection. The ejection statistics is strongly time-dependent, and it also varies with $d$ and $We$. Nevertheless, most of the dependence

to $d$ is removed when the rescaled ejection time $\tau_n$ (ejection time normalised by the time of maximal extension of the sheet) is considered. This is especially true during the sheet expansion, where droplets are mostly ejected radially starting from a time that increases with $d$. Droplets ejected at the same $\tau_n$ have approximately the same speed, which decreases as $\tau_n$ increases. Their mass distribution is more scattered, but it is bounded by a maximal ejectable mass that is an increasing function of $\tau_n$ only.

When the sheet retracts and collapses, both speed and mass distributions spread considerably (at least for the two most asymmetrical sheet scenarios) and do depend on $\delta$. This is partly due to the additional ejection of tangentially-ejected droplets, i.e. droplets ejected in a direction parallel to the sheet and normal to its retraction. In the most asymmetrical cases (small $d$), the final collapse of the sheet near to the edge triggers the out-of-plane ejection of a large number of tiny droplets.

We could then estimate the maximum horizontal distance that each ejected droplet would travel ballistically, as a function of its mass and ejection speed. The upper bound of this distance is independent of $\delta$ for the two most asymmetric scenarios. It can be predicted by considering the speed and maximum mass of droplets ejected during the sheet expansion only. Droplets ejected during the retraction and collapse of the sheet can go as far but not significantly farther. However, for the same travelled distance, their mass can be larger.

These results can be discussed in the context of the rain-induced dispersal of foliar pathogens. From an epidemiology point of view, each droplet ejected from an infected leaf is susceptible to carry some pathogenic content. The number, mass and ejection speed of these droplets are key inputs for the epidemiological models based on droplet ballistics [69]. The likelihood of infection certainly grows with each of these factors. Our experiments at $We \in [180, 2400]$ covered most of the range of Weber number experienced by raindrops ($We \in [28, 5800]$). We may therefore expect that our conclusions on the impact near a straight edge are still valid, at least qualitatively, for more complex impact scenarios encountered by raindrops on leafs. In particular, the number, the speed of the ejected droplets and their maximal travelled distance all increase with increasing $We$, but at the same time the maximal droplet mass decreases. The asymmetry of the sheet, here measured with $\delta$ and omnipresent in complex natural impacts, does not seem to increase the maximum distance travelled by the droplets. But it does increase their number and maximal mass at a given distance. It should consequently increase the likelihood that a droplet containing a critical amount of pathogens lands on a distant leaf, and so increase the overall dispersal speed of the disease.

Current mitigation techniques of foliar diseases, such as the intensive use of chemicals or genetically modified organisms cannot be solely relied upon on the long term [2, 70–75]. Some complementary approaches include polyculture [13, 76, 77] or integrated culture [71]. The risk of epidemics is a major factor to take into account in the optimisation of such crops [77]. Our work has showed how both $We$ and $\delta$ shape the statistics of ejected droplets upon raindrop impacts, and the subsequent risk of epidemics. Our results will hopefully be implemented in future ballistic-based epidemiological models.

## ACKNOWLEDGMENTS

The authors thank the FRIA/FNRS and USDA-NIFA Specialty Crop Research Initiative Grant Award No. MDW-2016-04938 and MIT REED and Edgerton Funds. S.L is grateful for the support of the Rotary Foundation. The authors also thank L. Tadrist and Y. Wang for fruitful discussions.

### 1. Droplet tracking and mass calculation

On each frame, all the objects detached from the main body of the sheet were considered as ejected droplets. Their area, perimeter and position with respect to the impact point was recorded. Their trajectory was then reconstructed. During this process, only objects that could be consistently tracked over at least five frames were considered. This condition removed fluid particles that either quickly merged with others, or that quickly fragmented. The ejection time of the droplets is defined as the time at which they were first detected. The ejection velocity $v$ is calculated from the first frames after ejection. Merging and fragmentation of droplets are common, especially during sheet retraction in the most asymmetrical scenarios (2 - 3). We chose to only consider as droplets the objects that either left the field of view before the end of the recording, or that were still present in its last frame. By doing so, we reduce the likelihood of counting multiple times the same fluid particle. However we also arbitrarily select large merged droplets instead of keeping the smaller droplets that were initially ejected. Furthermore, sometimes the residues of the collapsed sheet do not fully fragment by the time they leave the field of view.

Estimating the mass $m$ of the ejected droplets is challenging. Indeed, they are highly deformed when they pinch off from the liquid sheet, and they need some additional time to relax to a quasi-spherical equilibrium shape resulting from a balance of aerodynamic drag and surface tension [55]. This relaxation time is of the order of $r^2/\nu$, where $r$ is

such that $m/\rho = 4\pi r^3/3$. Moreover, droplet collisions are common, especially when the high asymmetry of the sheet leads to antagonist motions of the rim. It is therefore likely that the tracked droplets leave the field of view before they become spherical.

We here estimate the droplet volume $\Omega = m/\rho$ based on a combination of the perimeter $P$ and the area $A$ seen and measured on each image. A droplet pinching off from a fluid ligament is initially elongated, so at first order it can be approximated by a pill shape, i.e. a cylinder of length $L$ and radius $R$ surrounded by two spherical caps of radius $R$. When $L \gg R$, $\Omega$, $A$ and $P$ are proportional to $R^2L$, $RL$ and $L$, respectively, so the ratio $\Omega P/A^2$ should be constant. In general (for any $L$ and $R$),

$$\frac{\Omega P}{A^2} = \frac{2\pi x^2 + \left(2\pi^2 + \frac{8\pi}{3}\right) x + \frac{8\pi^2}{3}}{4x^2 + 4\pi x + \pi^2} \tag{27}$$

where $x = L/R$. The ratio $\Omega P/A^2$ indeed tends to a constant value of $\pi/2$ for an elongated pill ($x \gg 1$). In the other limit of a quasi-spherical pill ($x \ll 1$), $\Omega P/A^2 \simeq 8/3$, which is slightly larger. More complicated elongated shapes, such as when the sheet collapses after separation from the edge (scenario 4), could be seen as a sum of elongated droplets, and it is likely that their ratio $\Omega P/A^2$ remains in the range $[\pi/2, 8/3]$.

In order to estimate the droplet volume, we first calculate an approximation of $x$. Since $P = 2R(\pi + x)$ and $A = R^2(\pi + 2x)$, $x$ satisfies the second order equation:

$$x^2 + 2\left(\pi - \frac{P^2}{4A}\right) x + \pi\left(\pi - \frac{P^2}{4A}\right) = 0 \tag{28}$$

This equation admits a single positive solution $x$ when $P^2 \geq 4\pi A$ (the equality yields a spherical droplet). The volume is then calculated from equation 27.

In conventional image processing functions (e.g. in Matlab), $A$ is calculated as the sum of the selected pixels, while $P$ is calculated by joining the centres of the edge pixels. Consequently, $A$ is overestimated compared to $P$, which may erroneously result in $P^2 < 4\pi A$. This artefact may be corrected by removing the excess of area, i.e. by replacing $A$ by $A - \epsilon P/2$, where $\epsilon$ is the pixel size. This correction is sufficient to ensure $P^2 \geq 4\pi A$ for all droplets.

## Appendix A: Travelled distance: the aerodynamic wall

The ballistic trajectory $\mathbf{x}(t) = x(t)\mathbf{e}_x + z(t)\mathbf{e}_z$ of each ejected droplet can be computed from Newton's law, as a function of its mass $m$ and ejection speed $v$:

$$\begin{aligned} m\frac{d^2\mathbf{x}}{dt^2} &= -mg\mathbf{e}_z - 6\pi\mu_a r\frac{d\mathbf{x}}{dt}\left[1 + \frac{c}{100}Re^{2/3}\right] \text{ for } Re = \frac{2r\rho_a}{\mu_a}\left|\frac{d\mathbf{x}}{dt}\right| < 1000 \\ m\frac{d^2\mathbf{x}}{dt^2} &= -mg\mathbf{e}_z - \frac{3(1+c)}{125}\frac{\pi}{2}\rho_a r^2\frac{d\mathbf{x}}{dt}\left|\frac{d\mathbf{x}}{dt}\right| \text{ for } Re > 1000 \end{aligned} \tag{A1}$$

where $Re$ is the Reynolds number, $r = (3m/4\pi\rho)^{1/3}$ is the droplet radius, $c$ is a fitting parameter, and $\rho_a$ and $\mu_a$ are the density and dynamic viscosity of the air, respectively. We here consider $\mathbf{e}_x$ as the horizontal direction of ejection, and $x(t)$ is the distance travelled horizontally since ejection, no matter in which direction $\theta_v$. In (A1), the air drag is calculated with an approximation valid for spherical objects in a large range of Reynolds number (cf. similar models in Clift *et al.* [78]). A fit on experimental data from Duan *et al.* [79] yields $c \simeq 16$.

Owing to air drag, the horizontal speed decreases with time and $x(t)$ reaches an asymptotic value $\Psi = \lim_{t\to\infty} x$ called the aerodynamic wall [68].

First, (A1) is non-dimensionalised with characteristic timescale $T$ and length scale $L$ defined in the limit of small Reynolds number:

$$T = \frac{2\rho r^2}{9\mu_a}, \quad L = gT^2, \quad \mathbf{y} = \mathbf{x}/L, \quad \tau = t/T \tag{A2}$$

from which we obtain:

$$\begin{aligned} \frac{d^2\mathbf{y}}{d\tau^2} &= -\mathbf{e}_z - \left[1 + \frac{c}{100}\beta^{2/3}\left|\frac{d\mathbf{y}}{dt}\right|^{2/3}\right]\frac{d\mathbf{y}}{d\tau} \text{ if } \beta\left|\frac{d\mathbf{y}}{dt}\right| < 1000 \\ \frac{d^2\mathbf{y}}{d\tau^2} &= -\mathbf{e}_z - \frac{1+c}{1000}\beta\left|\frac{d\mathbf{y}}{dt}\right|\frac{d\mathbf{y}}{d\tau} \text{ if } \beta\left|\frac{d\mathbf{y}}{dt}\right| > 1000 \end{aligned} \tag{A3}$$

where the dimensionless parameter $\beta$ is defined as

$$\beta = \frac{mg\rho_a}{3\pi\mu_a^2} = \frac{4\rho_a\rho g r^3}{9\mu_a^2} \tag{A4}$$

This differential equation can be integrated, with an initial horizontal dimensionless speed

$$\left.\frac{d\mathbf{y}}{d\tau}\right|_{\tau=0} \cdot \mathbf{e}_x = u = \frac{9\mu_a}{2\rho g r^2} v \tag{A5}$$

### 1. Exact solution at low Reynolds number

There is an exact solution to (A3) at low Reynolds number, i.e. for droplets that are sufficiently small so $\beta \ll 1$. Equation A3 then simplifies into:

$$\frac{d^2\mathbf{y}}{d\tau^2} + \frac{d\mathbf{y}}{d\tau} = -\mathbf{e}_z \tag{A6}$$

Time-integration yields:

$$\mathbf{y} = \left(1 - e^{-\tau}\right)(u\mathbf{e}_x + \mathbf{e}_z) - \tau\mathbf{e}_z \tag{A7}$$

The maximum horizontal distance travelled is then:

$$y_\infty = \lim_{\tau\to\infty} \mathbf{y} \cdot \mathbf{e}_x = u \tag{A8}$$

or, in dimensional form:

$$\Psi_0 = \Psi(\beta \ll 1) = y_\infty L = \frac{2\rho r^2 v}{9\mu_a} \tag{A9}$$

The condition $Re < 1$ yields

$$\frac{2r\rho_a L}{\mu_a T} < 1 \Rightarrow \beta < 1 \tag{A10}$$

### 2. Numerical solution for any Reynolds number

The droplets ejected during the sheet fragmentation are in the range $m/M_0 \in [3\times10^{-6}, 3\times10^{-2}]$ (figure 21a), which corresponds to $r \in [0.035, 0.75]$ mm and $\beta \in [0.67, 6700]$. The ejection speed can reach 10 m/s, so the Reynolds number at ejection can be as high as 1000. Therefore we need to solve (A3 numerically).

The solution is represented for dimensionless size $\beta \in [10^{-4}, 10^7]$ and ejection speed $v \in [10^{-3}, 10]$ m/s, in figure 25. Once normalised by $\Psi_0$, the aerodynamic wall $\Psi$ does not depend on ejection speed $v$ anymore, except for very large speed (here $v = 10$ m/s) where $\Psi/\Psi_0$ can be twice smaller than at moderate speed. So in first approximation,

$$\frac{\Psi}{\Psi_0} = F(\beta) \tag{A11}$$

where $F(\beta) \to 1$ for $\beta \to 0$ and $F(\beta) \to 12/\sqrt{\beta}$ when $\beta \to \infty$.

The function $F(\beta)$ satisfies $F(0) = 1$ (low Reynolds limit), and it scales as $F \sim \beta^{-1/2}$ for $\beta \gg 1$ (high Reynolds limit). Since $\beta$ is only dependent on droplet size $r$ and not on speed $v$, the aerodynamic wall at a distance $\Psi$ is always approximately proportional to the ejection speed $v$.

[1] E.-C. Oerke, Journal of Agricultural Science **144**, 31 (2006).
[2] I. B. Pangga, J. Hanan, and S. Chakraborty, Plant Pathology **60**, 70 (2011).
[3] H. Fones and S. Gurr, Fungal Genetics and Biology **79**, 3 (2015).

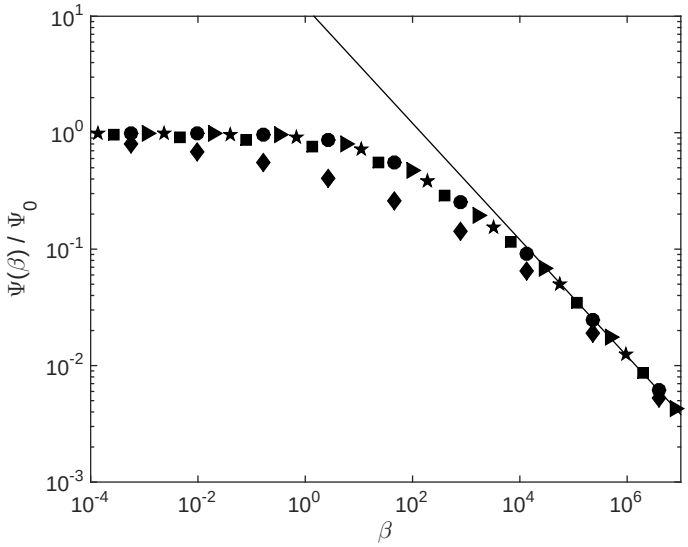


FIG. 25. Maximum travelled horizontal distance $\Psi$, as a function of the dimensionless droplet size $\beta$. Each symbol corresponds to a different ejection speed $v$: (◯) $v = 10^{-3}$ m/s, (▷) $v = 10^{-2}$ m/s, (★) $v = 10^{-1}$ m/s, (□) $v = 1$ m/s, (◇) $v = 10$ m/s. The solid line corresponds to $\Psi(\beta)/\Psi(0) \simeq 12\beta^{-1/2}$.


[4] R. D. Magarey, T. B. Sutton, and C. L. Thayer, Phytopathology **95**, 92 (2005).
[5] A. Dalla Marta, R. D. Magarey, and S. Orlandini, Agricultural and Forest Meteorology **132**, 84 (2005).
[6] A. Calonnec, J.-B. Burie, M. Langlais, S. Guyader, S. Saint-Jean, I. Sache, and B. Tivoli, European Journal of Plant Pathology **135**, 479 (2013).
[7] G. Garin, C. Fournier, B. Andrieu, V. Houlès, C. Robert, and C. Pradal, Annals of Botany **114**, 795 (2014).
[8] B. D. L. Fitt, H. A. McCartney, and P. J. Walklate, Annual review of phytopathology. **27**, 241 (1989).
[9] P. A. Paul, S. M. El-Allaf, P. E. Lipps, and L. V. Madden, Phytopathology **94**, 1342 (2004).
[10] G. N. Agrios, *Plant pathology* (London, 2005).
[11] P. Walklate, H. McCartney, and B. Fitt, Plant Pathology **38**, 64 (1989).
[12] X. Yang, L. V. Madden, L. L. Wilson, and M. A. Ellis, Phytopathology **80**, 1115 (1990).
[13] C. Gigot, S. Saint-Jean, L. Huber, C. Maumené, M. Leconte, B. Kerhornou, and C. de Vallavieille-Pope, Plant Pathology **62**, 1011 (2013).
[14] K. M. Reynolds, M. A. Bulger, L. V. Madden, and M. A. Ellis, Phytopathology (USA) **77**, 921 (1987).
[15] X. Yang, L. V. Madden, D. L. Reichard, R. Fox, and M. A. Ellis, Agricultural and Forest Meteorology **56**, 67 (1991).
[16] I. Sache, Agronomie **20**, 757 (2000).
[17] S. Pietravalle, F. Van Den Bosch, S. J. Welham, S. R. Parker, and D. J. Lovell, Agricultural and Forest Meteorology **109**, 171 (2001).
[18] T. Gilet and L. Bourouiba, Integrative and Comparative Biology **54**, 974 (2014).
[19] T. Gilet and L. Bourouiba, Journal of the Royal Society Interface **12**, 20141092 (2015).
[20] A. L. Yarin, Annual Review of Fluid Mechanics **38**, 159 (2006).
[21] M. Marengo, C. Antonini, I. V. Roisman, and C. Tropea, Current Opinion in Colloid and Interface Science **16**, 292 (2011).
[22] C. Josserand and S. T. Thoroddsen, Annual Review of Fluid Mechanics **48**, 365 (2016).
[23] A.-B. Wang and C.-C. Chen, Physics of Fluids **12**, 2155 (2000).
[24] C. Josserand and S. Zaleski, Physics of Fluids **15**, 1650 (2003).
[25] R. Rioboo, C. Bauthier, J. Conti, M. Voué, and J. De Coninck, Experiments in Fluids **35**, 648 (2003).
[26] M. Rein, Fluid Dynamics Research **12**, 61 (1993).
[27] B. Ray, G. Biswas, and A. Sharma, Journal of Fluid Mechanics **768**, 492 (2015).
[28] R. Rioboo, C. Tropea, and M. Marengo, Atomization and Sprays **11**, 155 (2001).
[29] M. Reyssat, A. Pépin, F. Marty, Y. Chen, and D. Quéré, Europhysics Letters **74**, 306 (2006).
[30] C. Antonini, A. Amirfazli, and M. Marengo, Physics of Fluids **24**, 102104 (2012).
[31] P. K. Unnikrishnan, V. Vaikuntanathan, and D. Sivakumar, Colloids and Surfaces A: Physicochemical and Engineering Aspects **459**, 109 (2014).
[32] D. Khojasteh, M. Kazerooni, S. Salarian, and R. Kamali, Journal of Industrial and Engineering Chemistry **42**, 1 (2016).
[33] Z. Levin and P. V. Hobbs, Phil Trans Roy Soc London Ser A. Math Phys Sci **269**, 555 (1971).
[34] S. Mandre, M. Mani, and M. P. Brenner, Physical Review Letters **102**, 134502 (2009).
[35] J. Palacios, J. Hernández, P. Gómez, C. Zanzi, and J. López, Experimental Thermal and Fluid Science **44**, 571 (2013).
[36] G. Riboux and J. M. Gordillo, Physical Review Letters **113** (2014), 10.1103/PhysRevLett.113.024507.
[37] G. Riboux and J. M. Gordillo, Journal of Fluid Mechanics **772**, 630 (2015).

[38] A. Rozhkov, B. Prunet-Foch, and M. Vignes-Adler, Physics of Fluids **14**, 3485 (2002).
[39] E. Villermaux and B. Bossa, Journal of Fluid Mechanics **668**, 412 (2011).
[40] C. Vernay, L. Ramos, and C. Ligoure, Journal of Fluid Mechanics **764**, 428 (2015).
[41] Y. Wang and L. Bourouiba, Journal of Fluid Mechanics **814**, 510 (2017).
[42] I. V. Roisman, Physics of Fluids **16**, 3438 (2004).
[43] I. V. Roisman, C. Planchette, E. Lorenceau, and G. Brenn, Journal of Fluid Mechanics **690**, 512 (2012).
[44] M. Reyssat, F. Pardo, and D. Quéré, EPL **87**, 36003 (2009).
[45] B. A. Malouin Jr., N. A. Koratkar, A. H. Hirsa, and Z. Wang, Applied Physics Letters **96**, 234103 (2010).
[46] V. Vaikuntanathan, R. Kannan, and D. Sivakumar, Colloids and Surfaces A: Physicochemical and Engineering Aspects **369**, 65 (2010).
[47] J. C. Bird, R. Dhiman, H.-M. Kwon, and K. K. Varanasi, Nature **503**, 385 (2013).
[48] D. H. Kwon, H. K. Huh, and S. J. Lee, Experiments in Fluids **55**, 1691 (2014).
[49] R. Zhang, P. Hao, and F. He, Langmuir **33**, 3556 (2017).
[50] J. C. Bird, S. H. Tsai, and H. A. Stone, New Journal of Physics **11**, 063017 (2009).
[51] Y. H. Yeong, J. Burton, E. Loth, and I. S. Bayer, Langmuir **30**, 12027 (2014).
[52] H. Fujimoto, S. Yoshimoto, K. Takahashi, T. Hama, and H. Takuda, Experimental Thermal and Fluid Science **81**, 136 (2017).
[53] G. Juarez, T. Gastopoulos, Y. Zhang, M. L. Siegel, and P. E. Arratia, Physical Review E - Statistical, Nonlinear, and Soft Matter Physics **85**, 026319 (2012).
[54] Y. Liu, M. Andrew, J. Li, J. M. Yeomans, and Z. Wang, Nature Communications **6**, 10034 (2015).
[55] E. Reyssat, F. Chevy, A.-L. Biance, L. Petitjean, and Quéré, EPL **80**, 34005 (2007).
[56] E. Villermaux and B. Bossa, Nature Physics **5**, 697 (2009).
[57] I. V. Roisman, C. M. Weickgenannt, A. N. Lembach, and C. Tropea, in *Proceedings of the 23rd Annual Conference on Liquid Atomization and Spray Systems, ILASS-Europe* (2010).
[58] C. Duez, C. Ybert, C. Clanet, and L. Bocquet, Physical Review Letters **104**, 084503 (2010).
[59] R. Rioboo, M. Marengo, and C. Tropea, Experiments in Fluids **33**, 112 (2002).
[60] A. L. Yarin and D. A. Weiss, Journal of Fluid Mechanics **283**, 141 (1995).
[61] I. V. Roisman, R. Rioboo, and C. Tropea, Proceedings of the Royal Society A: Mathematical, Physical and Engineering Sciences **458**, 1411 (2002).
[62] J. Eggers, M. A. Fontelos, C. Josserand, and S. Zaleski, Physics of Fluids **22**, 062101 (2010).
[63] H. Lastakowski, F. Boyer, A.-L. Biance, C. Pirat, and C. Ybert, Journal of Fluid Mechanics **747**, 103 (2014).
[64] N. Laan, K. G. De Bruin, D. Bartolo, C. Josserand, and D. Bonn, Physical Review Applied **2**, 044018 (2014).
[65] G. Lagubeau, M. A. Fontelos, C. Josserand, A. Maurel, V. Pagneux, and P. Petitjeans, Journal of Fluid Mechanics **713**, 50 (2012).
[66] F. Blanchette and T. P. Bigioni, Nature Physics **2**, 254 (2006).
[67] T. Gilet, K. Mulleners, J. P. Lecomte, N. Vandewalle, and S. Dorbolo, Physical Review E - Statistical, Nonlinear, and Soft Matter Physics **75**, 036303 (2007).
[68] C. Cohen, B. Darbois-Texier, G. Dupeux, E. Brunel, D. Quéré, and C. Clanet, Proceedings of the Royal Society A: Mathematical, Physical and Engineering Sciences **470**, 1 (2013).
[69] S. Saint-Jean, M. Chelle, and L. Huber, Agricultural and Forest Meteorology **121**, 183 (2004).
[70] R. N. Strange and P. R. Scott, Annual Review of Phytopathology **43**, 83 (2005).
[71] A. C. Newton, C. Gravouil, and J. M. Fountaine, Annals of Applied Biology **157**, 343 (2010).
[72] S. Chakraborty and A. C. Newton, Plant Pathology **60**, 2 (2011).
[73] R. C. Derksen, P. A. Paul, H. E. Ozkan, and H. Zhu, Applied Engineering in Agriculture **28**, 325 (2012).
[74] M. Enserink, P. J. Hines, S. N. Vignieri, N. S. Wigginton, and J. S. Yeston, Science (New York, N.Y.) **341**, 728 (2013).
[75] J. Sherman and D. H. Gent, Plant Disease **98**, 1024 (2014).
[76] M. S. Wolfe, Nature **406**, 681 (2000).
[77] T. Vidal, A.-L. Boixel, B. Durand, C. de Vallavieille-Pope, L. Huber, and S. Saint-Jean, Agricultural and Forest Meteorology **246**, 154 (2017).
[78] R. Clift, J. R. Grace, and M. Weber, *Bubbles, drops, and particles* (Academic Press, London, 1978).
[79] Z. Duan, B. He, and Y. Duan, Scientific reports **5**, 12304 (2015).